

A. Lyssoivan, D. Douai, J. Ongena, V. Philipps, F.C. Schüller, D. Van Eester,
T. Wauters, T. Blackman, V. Bobkov, S. Brezinsek, E. de la Cal, F. Durodié,
E. Gauthier, T. Gerbaud, M. Graham, S. Jachmich, E. Joffrin, A. Kreter,
V. Kyrytsya, E. Lerche, P. Lomas, F. Louche, M. Maslov, M-L. Mayoral,
V. Moiseenko, I. Monakhov, I. Pankratov, M.K. Paul, R.A. Pitts, V. Plyusnin,
G. Sergienko, M. Shimada, V.L. Vdovin and JET EFDA contributors

Simulation of ITER Full Field ICWC Scenario in JET: RF Physics Aspects

“This document is intended for publication in the open literature. It is made available on the understanding that it may not be further circulated and extracts or references may not be published prior to publication of the original when applicable, or without the consent of the Publications Officer, EFDA, Culham Science Centre, Abingdon, Oxon, OX14 3DB, UK.”

“Enquiries about Copyright and reproduction should be addressed to the Publications Officer, EFDA, Culham Science Centre, Abingdon, Oxon, OX14 3DB, UK.”

The contents of this preprint and all other JET EFDA Preprints and Conference Papers are available to view online free at www.iop.org/Jet. This site has full search facilities and e-mail alert options. The diagrams contained within the PDFs on this site are hyperlinked from the year 1996 onwards.

Simulation of ITER Full Field ICWC Scenario in JET: RF Physics Aspects

A. Lyssoivan, D. Douai, J. Ongena¹, V. Philipps³, F.C. Schüller⁴, D. Van Eester¹, T. Wauters¹,
T. Blackman⁵, V. Bobkov⁶, S. Brezinsek³, E. de la Cal⁷, F. Durodié¹, E. Gauthier², T. Gerbaud⁵,
M. Graham⁵, S. Jachmich¹, E. Joffrin², A. Kreter³, V. Kyrytsya¹, E. Lerche¹, P. Lomas⁵,
F. Louche¹, M. Maslov⁵, M-L. Mayoral⁵, V. Moiseenko⁸, I. Monakhov⁵, I. Pankratov⁸,
M.K. Paul⁹, R.A. Pitts¹⁰, V. Plyusnin¹¹, G. Sergienko³, M. Shimada¹⁰, V.L. Vdovin¹²,
and JET EFDA contributors*

JET-EFDA, Culham Science Centre, OX14 3DB, Abingdon, UK

¹ Association EURATOM-Belgian State, LPP-ERM-KMS, 1000 Brussels, Belgium

² Association EURATOM-CEA, CEA, IRFM, 13108 St Paul lez Durance, France

³ Association EURATOM-IEK-4, Forschungszentrum Jülich, 52425 Jülich, Germany

⁴ Under contract with ITER Organization, 13115 St. Paul lez Durance, France

⁵ Association EURATOM-CCFE, Culham Science Centre, Abingdon, OXON OX14 3DB, UK

⁶ Association EURATOM-IPP, Max-Planck Institut für Plasmaphysik, 85748 Garching, Germany

⁷ Association EURATOM-CIEMAT, Laboratorio Nacional de Fusión, 28040 Madrid, Spain

⁸ Institute of Plasma Physics, NSC KIPT, 61108 Kharkiv, Ukraine

⁹ National Institute of Technology Agartala, 799 055 West Tripura, India

¹⁰ ITER Organization, 13115 St. Paul lez Durance, France

¹¹ Association EURATOM-IST, Instituto de Plasmas e Fusão Nuclear, 1049-001 Lisboa, Portugal

¹² RRC Kurchatov Institute, Nuclear Fusion Institute, 123182 Moscow, Russia

* See annex of F. Romanelli et al, "Overview of JET Results",

(23rd IAEA Fusion Energy Conference, Daejon, Republic of Korea (2010)).

ABSTRACT.

ITER as a *superconducting* fusion machine needs efficient wall conditioning techniques for application in the presence of a *permanent high magnetic field* mainly for (i) reducing the in-vessel impurity content, (ii) surface hydrogen isotope exchange and (iii) controlling the in-vessel long term tritium retention. Encouraging results recently obtained with Ion Cyclotron Wall Conditioning (ICWC) in the present-day tokamaks and stellarators have raised ICWC to the status of one of the most promising techniques available to ITER for routine inter-pulse and overnight conditioning with the ITER main ICRF heating system in the presence of the permanent high toroidal magnetic field. This paper is dedicated to a milestone experiment in ICWC research: the first simulation of ICWC operation in an equivalent ITER full-field scenario and the assessment of the wall conditioning effect on the carbon wall in the largest present-day tokamak JET. We address in this paper the following main topics: (i) an analysis of the RF physics of ICWC discharges, (ii) the optimization of the operation of ICRF antennas for plasma startup and (iii) an outlook for the performance of ICWC in ITER using the ICRF heating system. Important operational aspects of the conventional ICRF heating system in JET (the so-called A2 antenna system) for use in the ICWC mode are highlighted: (i) the ability of the antenna to ignite the cleaning discharge safely and reliably in different gases, (ii) the capacity of the antennas to couple a large fraction of the RF generator power ($>50\%$) to low density ($\sim 10^{10}-10^{12} \text{ cm}^{-3}$) plasmas and (iii) the ICRF absorption schemes aimed at improved RF plasma homogeneity and enhanced conditioning effect. Successful optimization of the JET ICWC discharge parameters ($B_T = 3.3 \text{ T}, f = 25 \text{ MHz}$) resulted in a reliable operation of the JET A2 antennas and a high conditioning efficiency in a scenario imitating closely ITER full field operation ($B_T = 5.3 \text{ T}, f = 40 \text{ MHz}$) with the fundamental Ion Cyclotron Resonance for deuterium ($\omega = \omega_{cD+}$) located on-axis. Numerical modeling with the 3-D electromagnetic code Micro Wave Studio, a 1-D RF full wave code and a 0-D plasma code allows extrapolating the results obtained on JET and other present-day tokamaks to ITER and provides good prospects for the use of the ITER ICRF antennas for ICWC purposes.

1. INTRODUCTION

In ITER and other superconducting fusion devices, the presence of the permanent, high toroidal magnetic field will prevent using Glow Discharge Conditioning (GDC) between pulses [1-3]. An alternative is the Ion Cyclotron Wall Conditioning (ICWC) technique, based on Radio-Frequency (RF) discharge ignition and sustainment with conventional ICRF heating or ICWC dedicated antennas in the presence of B_T . This was recently demonstrated in present-day tokamaks [4-8] and stellarators [9-12] and summarized in Refs. [13,14]. The encouraging results obtained have promoted ICWC to the status of one of the most promising techniques available to ITER for routine inter-pulse and overnight conditioning of the first wall, in particular for recovery after disruptions, hydrogen isotope ratio control and fuel removal. The ability to operate in the ICWC mode has been confirmed as a functional requirement of the ITER main ICRF heating and current drive system [3,15].

This paper focuses mainly on a study of the RF physics aspects of ICWC discharges and the further development of a model consistently describing the process of ICRF plasma production. This study is aimed on the elaboration of safe and efficient operation of standard ICRF heating antennas in the ICWC mode: (i) the ability to safely and reliably ignite RF cleaning discharges in different gases, (ii) the possibility to couple a large fraction of the RF generator power ($>50\%$) to low density ($\sim 10^{10}\text{--}10^{12} \text{ cm}^{-3}$) plasmas and (iii) the development of RF power absorption schemes aimed at improved RF plasma homogeneity and enhanced conditioning effect. All these factors were identified as crucial to achieve the main ICWC target – to be an efficient conditioning technique for fusion reactors with superconducting coils. Upgrading of the earlier developed gas breakdown model [16-19] gave an impact on the selection of the principal antenna parameters (frequency, RF voltage / RF power, antenna phasing) and gas pressure range needed for safe operation of the ICRF system. Optimization of the antenna phasing and absorbed RF power by electrons in the regime of plasma waves excitation/absorption in plasmas containing multi-ion species resulted in a successful performance of the JET ICWC experiments with two standard A2 antennas ($B_T = 3.3 \text{ T}, f = 25 \text{ MHz}$) in a scenario simulating ITER full field ($B_T = 5.3 \text{ T}, f = 40 \text{ MHz}$) conditions: on-axis location of the fundamental Ion-Cyclotron Resonance (ICR) for deuterium, $\omega = \omega_{cD+}$. The experiments were done with the carbon wall in JET.

Finally, we assess the feasibility of ITER ICRF system operation in the ICWC mode with numerical modeling (3-D MWS electromagnetic code [20], 1-D RF full wave code [21] and 0-D plasma code [22]) and empirical extrapolation from the results obtained on the largest present-day tokamaks.

2. BASIC PRINCIPLES OF PLASMA PRODUCTION WITH STANDARD POLOIDAL ICRF ANTENNA: PRESENT STATUS

The initiation of ICRF discharges in a gas-filled toroidal vessel in the presence of a static toroidal magnetic field B_T results from the absorption of RF energy mainly by the electrons [17,23]. The parallel electric RF field $E_{||}$ (parallel to the B_T -field lines) is thought to be responsible for this process [16]. The neutral gas breakdown initiates from the acceleration in the $E_{||}$ -field of a few initial free electrons with rather low energy up to the ionization energy and subsequent electron-impact avalanche ionization. Usually, such initial electrons are present in the vacuum vessel as a background due to sporadic ionization events in the injected gas by cosmic and/or terrestrial radiation.

In this section we discuss basic aspects of (i) the $E_{||}$ -field generation in vacuum by conventional ICRF heating antennas, (ii) the gas breakdown and initial ionization and (iii) the RF plasma build-up and sustain the conditioning discharge in the regime of plasma wave excitation and absorption. For further analysis, we assume that the toroidal B_T -field is along the z-axis. We note also that throughout the text, Gaussian-cgs units will be employed.

2.1. GENERATION OF ANTENNA-NEAR $E_{||}$ -FIELD IN VACUUM

Electromagnetic wave propagation in vacuum satisfies the well-known dispersion relatio

$$\kappa^2 = \frac{\omega^2}{c^2}, \quad (1)$$

where κ is the wave vector, $\omega = 2\pi f$ with f the generator frequency and c is the speed of light in vacuum. In a uniform medium of infinite extent, all wave numbers are allowed and the spectrum $\omega(\kappa)$ is continuous. However, it is a common characteristic of bounded media (waveguides), that the spectrum of eigenmodes and eigenvalues is discrete [24]. As a result, even a carefully designed antenna array will excite a band of discrete modes. Therefore, the dispersion relation (1) in a torus with cylindrical cross section may be written in the following form [25]:

$$\kappa_r^2 = \omega^2 / c^2 - \kappa_z^2 - \kappa_\theta^2. \quad (2)$$

Here κ_r , κ_θ , κ_z are the wave vector components with $\kappa_z^2 = \frac{n^2}{R_0^2}$, $\kappa_\theta^2 = \frac{m^2}{r_0^2}$; R_0 and r_0 are the major and minor radii of the torus, respectively, and n and m the toroidal and poloidal mode numbers determined by the antenna κ_z and κ_θ spectra in vacuum. Depending on the dimensions of the vacuum vessel relative to the wavelength, the electromagnetic waves can either propagate or be evanescent. For most of the antenna toroidal/poloidal κ -spectrum in the typical ICRF band (~ 20 – 60 MHz), the electromagnetic waves (Electric (E) cylindrical modes) cannot propagate in the vacuum torus of the present-day *small-size* fusion machines ($\bar{r}_0 \approx 50$ – 136 cm, $R_0 \approx 165$ – 296 cm): $\kappa_r^2 = \omega^2/c^2 - \kappa_z^2 - \kappa_\theta^2 < 0$. Even the RF waves with the longest toroidal wavelength ($\kappa_z = 1/R_0$) or with infinite wavelength ($\kappa_z = 0$), which satisfy the propagation condition $\kappa_r^2 > 0$, only oscillate in front of the antenna ($\kappa_r r_0 < \pi$) but cannot propagate along the torus. The perpendicular wavelength of such waves is still larger than the cross-section of *present-day* tori. Hence, the free electrons may initially be accelerated up to the ionization energy in the *locally generated* antenna-near electric RF field $E_{||} \equiv E_z$.

It should note that in future large-size fusion machines like ITER, the electromagnetic waves can already propagate in vacuum torus in the mentioned ICRF band. Details of the latter regime will be analyzed in Section 4 of the present manuscript.

In the general case of an ICRF antenna with poloidal straps and a tilted Faraday Screen (FS) like in the case of the JET A2 antennas [26], the RF E -field in vacuum can be induced *electrostatically* and *inductively* [18].

The *electrostatic* E_z -component results from the RF potential difference between the central conductor and the side parts of the antenna box (antenna protection side RF limiters) revealing exponential decay in radial ($r \equiv x$) direction:

$$E_{zest}(r) \approx (V_{RF} / d) \exp(-\kappa_{z1} \Delta r). \quad (3)$$

Here V_{RF} is the maximum RF voltage on the central strap, d is the toroidal gap between the current

strap and the antenna box (Fig.1), $\kappa_{z1} = \pi/d$ is the inverse decay-length of the antenna-near field.

The *inductive* electric RF-field results from the RF voltage induced between FS bars by the time-varying magnetic flux generated by RF current in the antenna straps. This electric RF field may have a parallel component due to (i) a tilting position of the FS rods relatively to the B_T -direction (angle β) and (ii) a small magnetic deviation of the antenna straps from the perpendicular direction to the B_T -field line caused by the vertical component of the toroidal magnetic field ripples in the antenna vicinity (angle γ) or by the additionally imposed vertical magnetic field $B_V \equiv B_y \ll B_T$ (angle θ). The total *inductive* E_z -component of the antenna fringe field depends on these angles β, γ, θ , their mutual orientation and also decays in radial direction:

$$E_{zelm}(r) \approx [(V_{RF}/N)l_y] \sin(\beta \pm \gamma \pm \theta) \exp(-\kappa_{z2}\Delta r), \quad (4)$$

where N is the number of FS gaps, l_y is the poloidal width of FS gaps, l_z is the FS toroidal length-per-strap, $\kappa_{z2} = \pi/l_z$.

Such a simplified analytical description of the antenna-near E_z -field in vacuum was found in a good agreement with numerical simulations for real antenna configurations with the commercial 3-D electromagnetic code Micro Wave Studio (MWS) [20].

Details of the E_z -field structure typical for ITER multi-strap ICRF antenna with non-tilted FS are shown in Figs.2,3. Important points to note are:

- The E_z -field is maximum in the gaps between the antenna straps and side walls (septa) closer to the strap edge highlighting the *electrostatic* nature of the field (Fig.2a).
- The amplitude of the E_z -field decreases in the poloidal direction from a *maximum* value at the feeding point to *zero* at the grounding point (Fig.2a). The impact of such variation of the antenna-near E_z -field on gas breakdown will be discussed in Section 3.1.
- The field penetrates outside the antenna box through the gaps between the FS rods and shows a discrete character in the poloidal direction (Fig.2b).
- The amplitude of the parallel electric RF field decays exponentially in radial direction, $E_z(r) = E_0 \exp(-\kappa_z \Delta r)$, with the inverse decay-length of the antenna-near field κ_z determined by the antenna toroidal size and the current phasing between the antenna straps (Figs.2,3).
- In monopole phasing (Fig. 3a), the characteristic parallel length of the variation of the E_z -field outside of the antenna box in toroidal direction $L_{z1} = 2E_z/(dE_z/dz) l_z$ is much larger than the width of a single strap l_z , $L_{z1} \gg l_z$. It is comparable in dipole phasing $L_{z2} \geq l_z$ (Fig.3b).

2.2 Initial gas breakdown

The analytical/numerical analysis of the $E_{||} \equiv E_z$ -field generated by standard ICRF antenna with poloidal straps was used as a basis for the development of a model for the RF plasma production in toroidal magnetic fusion devices.

We will start a study of the neutral gas electrical breakdown in presence of the antenna-near RF

field from the formulation of equation of motion of free electron in an *inhomogeneous* RF electric field and consider only inhomogeneity along the field direction (z-direction). We will also use in our analysis a simple approach based on the concept of the “average electron” [27], i.e. an ensemble of electrons characterized by their velocity distribution function will be replaced by the same amount of electrons having an average velocity. Assuming a constant toroidal magnetic field B_T along the z-axis the parallel equation of motion for an “average electron” may be formulated in the following way [28]:

$$m_e \frac{d^2 z}{dt^2} = -eE_z(z)\cos(\omega t) - m_e \frac{dz}{dt} \bar{v}_c . \quad (5)$$

The first term of Eq.(5) at the right hand side describes the electron motion under the action of the *Lorentz force*, the second term the *friction force* (momentum loss of the electrons due to collisions with gas molecules or atoms with the effective collision frequency \bar{v}_c). An analytic treatment of the problem is possible when we apply a perturbation theory which comprises mathematical methods that are used to find an approximate solution to a problem starting from the exact solution of a *related* problem and adding to it “small” terms. Following this technique, we will write the solution of Eq.(3) in terms of a power series and retain terms up to second order, i.e. $z(t) \approx z_0 + z_1(t) + z_2(t)$, and identify z_0 as the starting position of the electron [29]. We further expand the spatial evolution of the electric field to first order in terms of a Taylor series:

$$E_z(z) \approx E_z(z_0) + z_1(t) \frac{dE_z(z_0)}{dz} , E_z(z_0) \gg z_1(t) \frac{dE_z(z_0)}{dz} . \quad (6)$$

Note that the second term in Eq.(6) is already of second order and no contribution from the $z_2(t)$ -solution is required. Using this approach we separate the motion of the electron, as suggested by Swanson [30], into:

- a fast oscillation motion slowed down by the mentioned above collisions

$$m_e \frac{d^2 z_1}{dt^2} = -eE_z(z_0) \cos(\omega t) - m_e \frac{dz_1}{dt} \bar{v}_c , \quad (7)$$

- a slow motion which describe an averaged drift of the electron oscillation center

$$m_e \left\langle \frac{d^2 z_2}{dt^2} \right\rangle = -e \langle z_1(t) \cos(\omega t) \rangle \frac{dE_z(z_0)}{dz} , \quad (8)$$

The first integral of Eq.(5) has the following solution:

$$v_{z1}(t) = \frac{dz_1}{dt} = -\frac{eE_{z0}}{m_e(\omega^2 + \bar{v}_c^2)} (\omega \sin(\omega t) + \bar{v}_c \cos(\omega t)) + \frac{eE_{z0} \bar{v}_c}{m_e(\omega^2 + \bar{v}_c^2)} \exp(-\bar{v}_c t) \quad (9)$$

We assume here that the electron starts motion from the rest ($v_{z1}(t_0) = 0$) and $E_{z0} = E_z(z_0)$. One can easily see that the first term of Eq.(9) describes a “stationary” oscillation velocity of the electron

and the second term gives its exponential time-decay induced by collisions. The second integral of Eq.(7) describes an oscillation amplitude of the electron:

$$z_1(t) = z_0 + \frac{eE_{z0}}{m_e\omega(\omega^2 + \bar{v}_c^2)} (\omega \cos(\omega t) - \bar{v}_c \sin(\omega t)) - \frac{eE_{z0}}{m_e(\omega^2 + \bar{v}_c^2)} \exp(-\bar{v}_c t) \quad (10)$$

Substituting Eq.(10) in the force equation (8) and averaging over $2\pi/\omega$ time-scale, we get:

$$m_e \left\langle \frac{d^2 z_2}{dt^2} \right\rangle = - \frac{e^2 E_{z0}}{2m_e(\omega^2 + \bar{v}_c^2)} \frac{dE_{z0}}{dz} = - \frac{e^2}{4m_e(\omega^2 + \bar{v}_c^2)} \frac{dE_{z0}^2}{dz} \quad (11)$$

This equation describes a slow drift motion of the electron toward the weak field area under the action of the *second order RF ponderomotive force* $F_p = - \frac{e^2}{4m_e(\omega^2 + \bar{v}_c^2)} \nabla_z(E_{z0}^2) = -\nabla_z \Phi_p$ and its associated *ponderomotive potential* $\Phi_p = \frac{e^2 E_{z0}^2}{4m_e(\omega^2 + \bar{v}_c^2)}$ *in the presence of collisions* with gas molecules and atoms with the effective collision frequency \bar{v}_c . We note here that the “potential” of the *ponderomotive force* is defined as the potential energy.

The energy can be transferred from the RF field to the electrons only through random collisions with the mentioned neutrals. Knowing the velocity of the electron fast oscillations (Eq.(9)), we can estimate a kinetic energy of the electron fast oscillations averaged over a cycle:

$$\langle W_e \rangle = \frac{m_e}{2} \langle v_{z1}^2(t) \rangle \approx \frac{e^2 E_{z0}^2}{4m_e(\omega^2 + \bar{v}_c^2)}. \quad (12)$$

If the average oscillation energy of the free electrons exceeds the ionization potential energy for the gas molecules i.e. $\langle W_e \rangle \geq \epsilon_i$, the gas ionization will occur. This inequality provides a *lower limit* to the amplitude of the parallel RF electric field required for neutral gas breakdown:

$$E_{z0} \geq E_{z0 \min} = (2/e) \sqrt{m_e \epsilon_i} \omega \sqrt{1 + \bar{v}_c^2 / \omega^2}. \quad (13)$$

Note that (i) the ponderomotive RF potential acts only near the antenna since at RF breakdown the waves do not propagate in the torus ($\omega_{pe} < \omega$, see Section 2.2) and (ii) the ponderomotive force derivation from Taylor expansion is valid for small/medium RF field amplitudes only,

$E_{z0} \gg z_1(t) dE_{z0}/dz$ (see Eq.(6)), when the oscillation amplitude of electrons in the RF field, $\langle z_1 \rangle = \langle v_{z1} \rangle / \omega$, is considerably smaller than the characteristic parallel length scale of the spatial variation of the E_z -field, $L_z = 2E_{z0}/(dE_{z0}/dz)$:

$$\frac{eE_{z0 \ max}}{\sqrt{2m_e \omega} \sqrt{\omega^2 + \bar{v}_c^2}} \ll L_z. \quad (14)$$

A more precise expression for the condition (14) was found by Carter for a linear variation in the

parallel RF electric field amplitudes of the form [16]:

$$|E_z(z)| \approx E_{z0} \frac{z}{(L_z/2)}, |z| < L_z/2. \quad (15)$$

We first consider an approximate formulation of the parallel equation of motion for an “averaged electron” in an inhomogeneous RF electric field retaining both solutions, fast oscillation and slow drift motions, and assuming $\bar{v}_c = 0$ for simplicity:

$$m_e \frac{d^2 z}{dt^2} = -eE_{z0} \cos(\omega t) - \frac{e^2}{4m_e \omega^2} \nabla_z (E_{z0}^2) \quad (16)$$

Substituting Eq.(15) into Eq.(16) and setting $\tau = \omega t$, we obtain the Mathieu equation

$$\frac{d^2 z}{d\tau^2} + (2\delta^2 + 2\delta \cos \tau) z = 0 \quad (17)$$

for which the condition for stable oscillatory solution is well known [31]. The parameter $\delta = eE_{z0}/m_e \omega^2 L_z$ is the stability parameter for the Mathieu equation that indicates when the concept of a “ponderomotive force” begins to break down. The trajectories of free electrons are no longer trapped in front of the antenna above the stability threshold [16]:

$$\delta \geq \frac{1}{4} - 2\delta^2 \text{ or } \delta > \frac{\sqrt{3}-1}{4} \approx 0.183. \quad (18)$$

For *low energy free electrons*, the ponderomotive potential may have two different transport effects depending on their position with respect to the RF ponderomotive potential well.

The electrons that are born from ionization events inside the antenna RF potential wells will remain *trapped* and oscillate for many RF periods thus giving rise to increased ionization efficiency. Therefore, we may consider the condition (18) as *an upper limit* to the parallel electric field which keeps the electrons trapped:

$$E_{z0} \leq E_{z0 \text{ max}} = (m_e/e) (0.18L_z) \omega^2 \sqrt{1 + (\bar{v}_c^2/\omega^2)}. \quad (19)$$

Taking into account the *lower* (13) and upper (19) limits on E_{z0} , the local neutral gas breakdown with the *trapped electrons* will be efficient if the amplitude of the antenna-near electric field meets the boundary condition:

$$(2/e) \sqrt{m_e \epsilon_i} \omega \sqrt{1 + (\bar{v}_c^2/\omega^2)} \leq E_{z0} \leq (m_e/e) (0.18L_z) \omega^2 \sqrt{1 + (\bar{v}_c^2/\omega^2)}. \quad (20)$$

An extension of the local breakdown condition (20) to the non-local (over torus) ionization with *non-trapped* electrons was undertaken by Schüller [32]. There are two types of *non-trapped* electrons:

1) The *escaped* electrons: when the value of the parallel component of the electric field E_z exceeds the $E_{z \max}$ value (19), the electrons escape from the antenna-near field region acquiring maximum available kinetic energy:

$$\langle W_{e \max} \rangle \approx \frac{e^2 E_{z0}^2 \max}{4m_e^2 (\omega^2 + \bar{v}_c^2)} . \quad (21)$$

2) The *repelled-out* electrons: the low energy electrons that are born outside the antenna region and approach it along the B_T -field lines will be repelled back by the antenna ponderomotive force. While being repelled back to a region where $E_z(z) \approx 0$, the electrons gain an amount of the ponderomotive potential energy, $(m_e \langle v_z^2 \rangle) / 2 = \Phi_p$, which is equal to the average kinetic energy of the oscillatory motion (Eq.(12)). Only those electrons that are repelled-out by the RF ponderomotive force with a field amplitude of $E_{z0} > E_{z0 \min}$ (Eq.(13)) will contribute to ionization events.

The ionization frequency for *trapped and non-trapped* electrons obtained by averaging the electron collisional ionization cross-section over an RF period can be represented as a function of the ratio E_z / f [32] and is shown in Fig.4 for the case of hydrogen gas. From this figure it becomes clear that the differences in ionization frequency close to and far from the antenna are not dramatic. However the toroidal length outside the antenna area, $(2\pi R_0 - L_z)$, is much larger than the one inside, L_z , and therefore the electron multiplication due to non-trapped electrons may be comparable or even larger than the contribution due to trapped electrons. Figure 5 shows the gas breakdown diagram for both *trapped* and *non-trapped* electrons in the parameter space “electric field – frequency” for the JET A2 antennas. The general tendency predicted by the present model is that the higher the operation frequency, the higher the amplitude of the E_z -component of the electric field needed to ionize the gas and the broader the ionization zone with the electrons trapped and repelled from the antenna location. From this analysis we conclude that both, *escaped* and *repelled* electrons with energies exceeding the energy can initiate ionization anywhere in the torus, away from the antenna-near field, in addition to ionization in front of the antenna with the *trapped* electrons. This conclusion is in agreement with the experimentally observed toroidal symmetry of the line-integrated H_α emission (Balmer-lines in the visible spectrum) from ICWC plasmas measured in different toroidal/poloidal locations [18].

The model also predicts that the gas breakdown cannot be achieved with ICRF antennas in the low frequency range below a certain threshold defined by the parameter L_z characterizing the spatial variation of antenna E_z -field (for the given A2 antenna geometry and monopole phasing this frequency is around 3 MHz, see Fig.5): all electrons will be expelled/repelled-out from the antenna by the ponderomotive force before they accelerate to the ionization energy of the gas in the torus. This mechanism may explain the failure to produce RF plasmas in the stellarator U-1M at any amplitude of the E_z -field [33] at frequencies below 1.0 MHz. One should mention that (i) if the electrical breakdown condition (Eq.(18)) is satisfied, the $E_{z \max}$ -line shown in Fig.5 separates the ionization zones with *trapped* and *non-trapped* electrons only formally and (ii) the breakdown conditions may be located at different radii with respect to the antenna strap surface depending on

the applied RF voltage. The role of the trapped electrons in safe operation of ICRF antenna in the plasma production mode and details of the radial location of the gas breakdown zone using the JET A2 antennas will be discussed in Section 3.

2.3. Excitation/absorption of plasma waves and plasma density build-up over the torus

We consider in what follows the generation of waves in a plasma cylinder folded up to a torus and assume that the toroidicity is small, $r \ll R_0$. Here r is the plasma minor radius, R_0 is the plasma major radius. We assume that the plasma density and temperature are functions of the radius r and the variation of the toroidal magnetic field due to toroidicity is weak,

$$B_T \equiv B_z = B_0 \frac{R_0}{R} = \frac{B_0}{1 + (r/R_0) \cos\theta}.$$

The plasma will be treated as an anisotropic dielectric with a “cold plasma” ($\omega / (\sqrt{2}\kappa_{||}) \gg v_{Te}$) dielectric tensor

$$(\varepsilon_{ij}) = \begin{pmatrix} S & -iD & 0 \\ +iD & S & 0 \\ 0 & 0 & P \end{pmatrix} \quad (22)$$

with the following components [24]:

$$S = \frac{1}{2}(R+L), D = \frac{1}{2}(R-L), R = 1 - \sum_s \frac{\omega_{ps}^2}{\omega(\omega + \omega_{cs})}, L = 1 - \sum_s \frac{\omega_{ps}^2}{\omega(\omega - \omega_{cs})}, P = 1 - \sum_s \frac{\omega_{ps}^2}{\omega^2}. \quad (23)$$

Here $\omega_{pe} = (4\pi n_e e^2 / m_e)^{1/2}$, $\omega_{pi} = (4\pi n_i Z^2 e^2 / m_i)^{1/2}$ are the electron and ion plasma frequencies, $\omega_{ce} = eB_0 / m_e c$, $\omega_{ci} = ZeB_0 / m_i c$ are the electron and ion cyclotron frequencies, Z is the charge state. The dispersion relation that relates the perpendicular refractive index $N_\perp = \kappa_\perp c/\omega$ and the parallel refractive index $N_{||} = \kappa_{||} c/\omega$ to the frequency has the form of bi-quadratic equation [24,34]:

$$SN_\perp^4 - [(S-N_{||}^2)(S+P) - D^2]N_\perp^2 + P[(S-N_{||}^2)^2 - D^2] = 0. \quad (24)$$

Here “perpendicular” and “parallel” indexes are related to the toroidal magnetic field B_T . Since $N_{||}$ is determined by the antenna spectrum and ω is fixed by the generator, Eq.(22) can be solved for N_\perp^2 . Noting that ω_{pe}^2/ω^2 is much larger than other quantities in Eq.(24) it can be considerably simplified. The two solutions of the dispersion relation then may be approximated by *slow wave* (SW) and *fast wave* (FW) solutions [24,34]:

$$\kappa_{\perp SW}^2 \approx \frac{\omega^2}{c^2} \frac{(S-N_{||}^2)P}{S} \quad (25)$$

$$\kappa_{\perp FW}^2 \approx \frac{\omega^2}{c^2} \frac{(S-N_{||}^2)^2 - D^2}{S - N_{||}^2}. \quad (26)$$

We first consider cut-off densities (thresholds for the excitation, $\kappa_{\perp}^2=0$) and range of the propagation of the plasma waves, $\kappa_{\perp}^2>0$, in terms of SW and FW depending on the plasma density in the ion cyclotron range of frequencies (ICRF), $\omega_{ci}<\omega<\omega_{ce}$. The lowest density at which plasma wave can be excited corresponds to the SW cut-off frequency, $\kappa_{\perp SW}^2=0 \rightarrow P=0$, which is determined by the electron plasma frequency ω_{pe} [23,24]:

$$\omega^2 = \omega_{pe}^2 + \omega_{pi}^2 \approx \omega_{pe}^2, m_e \ll m_i. \quad (27)$$

For the generator frequency $f \approx 32.5$ MHz (typical for tokamaks JET, TEXTOR, ASDEX Upgrade) and deuterium gas we obtain $n_{e-cr}^{(1)} \approx 1.3 \times 10^7$ cm⁻³. Plasma with density $n_e < n_{e-cr}^{(1)}$ will flow along the toroidal magnetic field lines and will not disturb the RF field near the antenna. Under natural conditions, ω_{pe} should be merely considered as the time scale for restoring charge neutrality distorted by a collective displacement of the electrons from the ion background rather than the frequency for a regular free plasma oscillation as the latter will not be stable in a chaotic medium. However, if the plasma is subjected to a well-defined external perturbation like an electromagnetic wave excited by the antennas, a precisely defined driven oscillation can be maintained in principle indefinitely.

If $\kappa_{\perp SW} r > \pi$, the SW can start propagating along the torus and transfer energy to the electrons, causing further volume ionization of the neutral gas and plasma build-up in the density range $n_{e-cr}^{(1)} < n_e < n_{e-cr}^{(2)}$. The critical density $n_{e-cr}^{(2)}$ is determined by the cold plasma or the lower-hybrid resonance (LHR) condition, $\kappa_{\perp SW}^2 \rightarrow \infty$ ($S=0$):

$$\omega^2 = \omega_{LH}^2 \approx \omega_{ci}^2 + \frac{\omega_{pi}^2}{1 + \omega_{pe}^2 / \omega_{ce}^2} \approx \omega_{ci}^2 + \omega_{pi}^2, \quad \omega_{pe}^2 \ll \omega_{ce}^2. \quad (28)$$

At $n_e \approx n_{e-cr}^{(2)} \approx 3.5 \times 10^{10}$ cm⁻³ ($f=32.5$ MHz, $B_T=2.24$ T, deuterium, parabolic density profile), a zone with LHR appears at the plasma core, and as the density is raised further up this resonance shifts to the Low Field Side (LFS) plasma edge. The SW does not penetrate into a dense plasma ($\omega > \omega_{LH}$), where $n_e < n_{e-cr}^{(2)}$ and is absorbed by electrons in the peripheral plasma.

At higher density, $n_e \approx n_{e-cr}^{(3)} > n_{e-cr}^{(2)}$, the fast magneto-sonic wave (FW), Eq.(26), becomes propagating. The density threshold for the FW excitation $n_e \approx n_{e-cr}^{(3)}$ is determined by the LFS (antenna side) cut-off frequency for the FW:

$$\kappa_{\perp FW}^2 = 0 \rightarrow (R - N_{\parallel}^2)(L - N_{\parallel}^2) = 0 \rightarrow (R - N_{\parallel}^2) = 0 \quad (29)$$

Recalling that $\omega_{ci} < \omega < \omega_{ce}$ and that the condition for charge neutrality of deuterium plasmas may be written in the Stix's form [24]: $\frac{\omega_{pe}^2}{\omega_{ce}} = -\frac{\omega_{pi}^2}{\omega_{ci}}$, we obtain the following FW cut-off condition:

$$\omega_{pi}^2 = \left(\frac{\kappa_{\parallel}^2 c^2}{\omega^2} - 1 \right) \omega_{ci} (\omega + \omega_{ci}). \quad (30)$$

Note however that the FW cutoff frequency depends strongly on the κ_{\parallel} values determined by the antenna spectrum contrary to the SW cutoff frequency, Eq.(27). Consequently there is a large difference in the $\langle n_{e-cr}^{(3)} \rangle$ values depending on the antenna current spectrum, which in the case of a multi-strap antenna depends on the relative phasing of the currents in the individual straps. E.g. for TEXTOR ICRF antenna, $\langle n_{e-cr}^{(3)} \rangle \approx 6.9 \times 10^{10} \text{ cm}^{-3}$ for *monopole* phasing at $f=32.5\text{MHz}$ (with dominant $\kappa_{\parallel} = n_{\text{tor}} / R_0 \approx 0.01 \text{ cm}^{-1}$, for toroidal mode number $n_{\text{tor}} = 2$) and $\langle n_{e-cr}^{(3)} \rangle \approx 2.7 \times 10^{12} \text{ cm}^{-3}$ (for *dipole* phasing at $f=32.5\text{MHz}$ with dominant $\kappa_{\parallel} \approx 0.06 \text{ cm}^{-1}$, $n_{\text{tor}} = 10$), respectively. These estimates indicate the presence of a gap in the plasma density between the upper limit for SW propagation ($n_{e-cr}^{(2)}$) and threshold for FW excitation ($n_{e-cr}^{(3)}$). The gap in density becomes large (about two orders of magnitude) in the case of a double strap antenna operated with straps in (0π) -phasing. As a result, a prompt and robust RF plasma build-up up to a density $n_{e0} \approx (3 \div 6) \times 10^{12} \text{ m}^{-3}$ as observed in the experiments [18] cannot be explained taking into account the energy deposition by the SW and FW in the *cold inhomogeneous plasma approximation*.

However considering the *finite ion temperature approximation* (finite-Larmor-radius formalism, $\kappa_{\perp} \rho_i \neq 0$), mode conversion of the SW ($\omega > \omega_{pi}$) into an Ion Bernstein Wave (IBW) ($\omega < \omega_{pi}$) can occur in the vicinity of a “cold LHR” ($\omega \approx \omega_{pi}$). This mode propagates towards higher density regions ($\omega < \omega_{pi}$) where the IBW dispersion relation for the frequency range $\omega_{ci} < \omega \leq 2\omega_{ci}$ may be approximated in the form [35]:

$$\kappa_{IBW}^2 \approx \sum_i \frac{\omega_{pi}^2}{\omega^2 - \omega_{ci}^2} \left(\sum_i \frac{3\omega_{pi}^2 (kT_i/m_i)}{(4\omega_{ci}^2 - \omega^2)(\omega^2 - \omega_{ci}^2)} \right)^{-1}. \quad (31)$$

Here k is Boltzmann’s constant. As follows from Eq.(31), the IBW is a small-scale wave: $\kappa_{\perp} \rho_i \approx 0.4$ during the ionization and the density build-up phase (e.g. again for TEXTOR ICWC plasmas with $n_{e0} \approx 4.0 \times 10^{10} \text{ cm}^{-3}$, $T_i \approx 5\text{eV}$, at $f=32.5\text{MHz}$ and $B_T=2.24\text{T}$). The IBW perpendicular wave-vector κ_{\perp} is a weak function of the density and is practically independent of the antenna κ_{\parallel} -spectrum.

The dispersion relation $D(\mathbf{k}, \mathbf{r})=0$ for Maxwellian plasmas was studied numerically using a 1-D dispersion solver [36], which takes into account finite temperature effects. In addition to the FW and SW, it describes the IBW which are absent in the cold plasma description. As an illustration, we show in Fig. 6 the basic plasma wave dispersion diagram for plasma in TEXTOR at high and low B_T . One can clearly see that for the chosen plasma density and antenna *dipole* phasing (dominant $\kappa_{\parallel} = 0.06 \text{ cm}^{-1}$) the FW does not propagate at high B_T , $\text{Re}(\kappa_{FW}^2) < 0$. At low B_T , the FW tunnels through the evanescent region from the antenna location on the LFS and starts propagating to the plasma core, $\text{Re}(\kappa_{FW}^2) > 0$. Additionally, 4 higher harmonic cyclotron resonances ($\omega / \omega_{cD+} = 7 - 10$) appear over the plasma cross-section. They separate the plasma into 5 regions in which 5 higher frequency branches of the IBW are propagating.

An efficient plasma build-up and sustainment of the RF discharge relies on the dissipation of the RF power on the electrons. Because of the very low plasma temperature during the ionization phase, $T_e \approx (3-5)$ eV [5,17,37], the RF power is expected to be indeed dissipated mostly by electrons via elastic and non-elastic collisions with gas molecules, atoms and ions. The collisional damping is rather strong for the SW as $\text{Im } \kappa_{\perp\text{SW}} / \kappa_{\perp\text{SW}} \sim v_{ei} / \omega$, and inefficient for direct interaction of the FW with the electrons because $\text{Im } \kappa_{\perp\text{SW}} / \kappa_{\perp\text{SW}} \sim (v_{ei} / \omega)(m_e / m_i)$ [34]. The latter may be improved through conversion of the FW to the SW and IBW if $\omega > \omega_{ci}$ or by conversion at the Alfvén resonance if $\omega < \omega_{ci}$. The absorption and coupling by non-linear mechanisms is also possible [38]. The wave absorption via electron Landau damping mechanism becomes efficient at much higher electron temperatures ($T_e > 100$ eV at $f=25$ MHz and $\kappa_{\parallel} \approx 0-0.06$ cm⁻¹) which are not relevant for wall conditioning. The plasma build-up and sustainment can be obviously understood as a progressive excitation of the waves in plasmas through a progressively rising density, governed by the antenna κ_{\parallel} -spectrum of the radiated power, $P_{\text{RF}}(\kappa_{\parallel})$. Such a non-resonant (collisional) coupling of the RF power allows ICRF plasma production at any B_T . This statement from theory was clearly confirmed during pioneering RF plasma experiments in the tokamak TEXTOR [18]. Low B_T plasma production scenarios could be important for ICWC operation during e.g. the commissioning phase of ITER.

3. JET ICRF A2 antenna operation in ICWC mode

3.1. Antenna safety considerations and ICWC operational window

A major concern for ICRF antenna operation in plasma production mode is to prevent deleterious arcing events and plasma ignition inside the antenna box. To find out if such risks exist, we plot in Figs.7,8 the radial locations of the RF breakdown zones for trapped and non-trapped electrons for different frequencies, RF voltages at the antenna straps and relative phasings between straps for the JET A2 antennas. The diagrams show clearly that electrical breakdown of gas with *trapped*, *repelled-out* and *escaped* electrons can be achieved in a wide range for the generator frequency and RF voltage. One should notice that as the E_z -field decays away from the antenna surface in vacuum (see Section 2), there will always be regions where the E_z -field fulfills the gas breakdown condition, Eq.(13). Analysis of the H₂ ionization rate in terms of the ratio E_z/f [kV/mMHz] (Fig.3) shows that ionization with *locally trapped* electrons ($(E_z/f)_{trap} \approx (0.4-1.9)$) and *non-trapped* (*repelled-out*) electrons ($(E_z/f)_{rep} \approx 0.3-1.4$) becomes dominant for the parameter range applied in Figs.7, 8. The *non-trapped* (*escaped*) electrons ($1.0 < (E_z/f)_{esc} < 3.0$) are inefficient for ionization because of getting too high energy (1 keV $< W_{e-esc} < 10$ keV) [39].

The benefit of using monopole phasing (0000) compared to super-dipole phasing (00ππ) is clear as the breakdown zone involving the *trapped* and *non-trapped* (*repelled-out*) electrons is much larger and results thus in a shorter breakdown time [40]. Also the *trapped electrons* can play an important role for the safe operation of the antenna because:

- (1) The penetration of the gas breakdown zone inside the antenna box can be changed with the antenna frequency or the RF voltage (see Fig.8);
- (2) The trapped electrons dominantly populate the low energy part of the distribution ($10\text{eV} < \bar{W}_{e-trap} < 2000\text{eV}$) which is very efficient for (i) electron collisional ionization [39] and for (ii) secondary electron emission based on the electron resonance multipactor effect [41, 42].

For a safer operation of the antenna in plasma production mode the breakdown zone could be shifted out of the antenna box by e.g. increasing the RF voltage on the straps. However, the RF voltage at the antenna straps shows a variation in the poloidal direction from a maximum value at the feeding point to zero at the grounding (Fig.2a). As a result, the breakdown zone for trapped electrons may be shifted out of the antenna box only locally in the poloidal direction, e.g. in the vicinity of the feeding point, as demonstrated in Figs.7,8. But ionization zones with relevant amplitudes for gas breakdown, $E_z \geq E_{z\min} \approx 3 \text{kV/m}$ at $f=25 \text{MHz}$ (Fig.7) or $E_z \geq E_{z\min} \approx 4.8 \text{kV/m}$ at $f=40 \text{MHz}$ (Fig.8), will inevitably be present inside the antenna box due to the poloidal variation of the RF voltage. Operation at lower frequency can only reduce a critical range of the variation of RF voltage along the antenna strap that meets the breakdown condition with trapped electrons inside the antenna box but not eliminate the ionization zone completely. For example, operation with $V_{RF\text{-strap}} = 15 \text{kV}$ at the feeding point of JET A2 antenna results in ~ 2 times narrower critical range of RF voltage variation at 25 MHz compared to 40 MHz: $0.2 \text{kV} < V_{RF(25MHz)} < 6 \text{kV}$ versus $0.3 \text{kV} < V_{RF(40MHz)} < 15 \text{kV}$.

How to achieve a safe operation in such non-trivial conditions? The third parameter that can be varied (in addition to RF field amplitude and frequency) is the gas pressure in the torus. The breakdown model (Eqs.(19,20)) predicts a very weak dependence on the gas pressure in the torus due to low collisionality, $v_c \ll \omega$, for a large range of ICRF frequencies ($\sim 20\text{--}60 \text{MHz}$) at gas pressures typical for ICWC operation ($10^{-5}\text{--}10^{-3} \text{Pa}$). According to this model therefore, the radial location of the breakdown zone can only be shifted towards the antenna strap at very high gas pressures ($p \geq 10 \text{ Pa}$), which are atypical for ICWC operation and for which $v_c \geq \omega$. This prediction is in clear contradiction with the experimentally observed gas pressure threshold at $p \geq 0.1 \text{ Pa}$ above which the ICRF antenna cannot operate in the ICWC mode due to regularly happening arcing events inside the antenna box [18]. A different model was developed by Schüller [32], in which he assumes that plasma formation in front of the antenna takes place when the residence time of the electrons oscillating in the inhomogeneous E_z -field in front of the antenna is longer than the characteristic time for gas ionization, $t_{resid} > t_{ioniz}$. Extending this hypothesis to RF-field amplitudes present inside the antenna box (see Fig.2a) we obtain the following upper limit for the concentration of neutrals (i.e. gas pressure) inside the antenna box above which arcing and plasma formation can happen:

$$n_0 < \frac{eE_z}{\sqrt{2m_e\omega}} \cdot \frac{1}{L_{z\text{ ant}} < \sigma v >_{ioniz\text{-max}}}, (v_{e-n} \ll \omega). \quad (32)$$

Here E_z is the amplitude of antenna field oscillating with frequency ω , $L_{z\ ant}$ is the antenna toroidal size, $\langle\sigma v\rangle_{ioniz\text{-max}}$ is the maximum value of the electron collisional ionization rate for the gas present in the torus. It is clearly seen from Eq.(32) that the RF electric field E_z is a crucial factor determining the pressure safe limit. The generation of arcs and very likely plasma breakdown inside the antenna box can be initiated if its amplitude is close to the lower threshold for breakdown, $E_z = E_{z0\ min}$ (see Eq.(13)) at which $E_{z0\ min}/\omega = const$ for the given gas. Substituting Eq.(13) into Eq.(32) we obtain finally the following constraint on the pressure range inside antenna box as a function of the antenna size , gas ionization potential and electron collisional ionization rate:

$$p \text{ [Pa]} < 2.46 \times 10^{-7} \frac{\sqrt{\varepsilon_{ioniz}}}{L_{z\ ant} \langle\sigma v\rangle_{ioniz\text{-max}}}. \quad (33)$$

The RF field amplitude and frequency are implicitly present in Eq.(33) to meet the threshold for breakdown defined by Eq.(13). For the case of the JET A2 antenna operated in hydrogen or deuterium (H_2 electron collisional ionization rate $\langle\sigma v\rangle_{ioniz\text{-max}} \approx 4 \times 10^{-8} \text{ cm}^3/\text{s}$ [39]), ionization potential for molecules $\varepsilon_{ioniz} = 15.2 \text{ eV}$, $L_{z\ ant} \approx 4 \times 36 \text{ cm}$), Eq.(33) indeed indicates that one should avoid hydrogen torus (antenna) pressure values in excess of 0.17 Pa.

Therefore, safe antenna operation for ICWC applications implies the following operational recipes:

- Antenna baking, vacuum conditioning and extra gas pumping from the antenna box and vacuum transmission line – in order to keep the gas pressure inside antenna box below a safe limit.
- Selecting the lowest frequency consistent with ICWC operation.
- Applying the RF voltage/power at strongly reduced pressure before the gas injection (Eq. (33)) and with a ramp-up time shorter than the gas breakdown time in order to initiate ignition outside the antenna box.

To simulate an ITER full-field operation scenario ($B_T=5.3 \text{ T}$ and 40–55 MHz frequency band for the ITER ICRF system) whilst taking into account safety considerations and tokamak operational constraints in JET, the JET ICWC experiments were performed selecting the following parameters: $f=25 \text{ MHz}$ and $B_T=3.3 \text{ T}$ in order to keep the same ratio $f/B_T \approx 7.6 \text{ MHz/T}$ as in ITER (40 MHz at 5.3 T) with resonance condition for deuterium $\omega = \omega_{cD+}$ on-axis. Two of the four A2 ICRF antennas in JET, antenna **C** ($f_{A2-C}=26.06 \text{ MHz}$) and antenna **D** ($f_{A2-D}=25.21 \text{ MHz}$) each having four straps, were operated in *monopole* (0000) or *super-dipole* (00 $\pi\pi$) phasing to generate ICWC discharges in He, D_2 or a mix of both. Adapted gas inlet programming and the JET cryopumps were used to keep the gas pressure during the RF pulse ($\geq 8 \text{ s}$) in the range $2 \times 10^{-3} \text{ Pa}$. This low pressure is far below the limit predicted by Eq.(33) but was imposed by JET operational constraints in order to avoid arcing inside the Vacuum Transmission Line (VTL) as the VTL-pressure is coupled to the torus pressure. To extend the ICWC plasma in vertical direction and push it down towards the divertor area, an additional vertical magnetic field B_V between 3 and 30 mT in the “barrel” shaped configuration was also applied [43]. A schematic layout of the JET ICRF antennas and diagnostics involved in the ICWC experiment is shown in Figure 9.

3.2. Coupling RF power to low density ICWC plasmas

The plasma production scheme described in Section 2 is intended for a sustained ICWC discharge and assumes that the ICRF antenna couples the RF power to the plasma with a sufficiently high efficiency during all phases of the discharge. Here we define the antenna-plasma coupling efficiency as the fraction of the generator power coupled to the plasma, $\eta = P_{RF-pl} / P_{RF-G}$. The conventional ICRF antenna with poloidal straps is designed for heating of dense ($n_e > 10^{13} \text{ cm}^{-3}$) target plasmas using *FW excitation* with high coupling efficiency ($\eta > 0.9$). The use of this antenna for RF plasma production, but with the “plasma heating settings” (high κ_z -spectrum of the radiated RF power), resulted in poor coupling ($\eta_0 \sim 0.2 - 0.3$) to the low density RF plasmas $n_e \sim 10^{10} - 10^{11} \text{ cm}^{-3}$, at which FW is typically non-propagating (see Fig.6a). To improve the coupling to such low density plasmas *FW excitation in low density plasmas* is enhanced by using [44]: (i) phasing of the antenna such that low κ_z values dominate in the spectrum of the radiated RF power, (ii) FW-SW-IBW mode conversion (MC) in RF plasmas with two ion species, (iii) operation at High Cyclotron Harmonics (HCH), typically $\omega \approx 10\omega_{ci}$. The first solution (adapting the antenna phasing) results in a dramatic reduction (of about two orders) in the threshold density for FW excitation, (Eq. (21), with the JET A2 antennas ($f=25 \text{ MHz}$, $B_T=3.3 \text{ T}$, deuterium gas in the torus) when changing the phase of the RF current in the antenna straps from $0\pi0\pi$ -phasing ($n_{e-FW-dipole} \approx 1 \times 10^{13} \text{ cm}^{-3}$, $\kappa_{z28} \approx 0.07 \text{ cm}^{-1}$) to 0000 -phasing ($n_{e-FW-monopole} \approx 6 \times 10^{10} \text{ cm}^{-3}$, $\kappa_{z3} \approx 7.5 \times 10^{-3} \text{ cm}^{-1}$), respectively. The JET ICWC experiments have clearly demonstrated that indeed the antenna coupling efficiency strongly increased with monopole phasing (>50%) at which FW excitation was possible (Fig.10) thus confirming similar results earlier obtained in TORE SUPRA [40].

A comparison for the same experimental conditions between *monopole* (0000) and *super-dipole* ($00\pi\pi$) resulted in a higher coupled power (230kW vs. 65kW) and better radial/poloidal homogeneity of ICWC plasmas for *monopole* phasing (A2 Antennas C and D, $P_{RF-G \text{ tot}} = 2 \times 300 \text{ kW}$, (He+D_2)-plasma, $p_{\text{tot}} \sim 2 \times 10^{-3} \text{ Pa}$, $B_T = 3.3 \text{ T}$, $B_V = 30 \text{ mT}$). The better coupling in monopole phasing due to the beneficial wave spectrum was also enhanced by the resulting increase in density. It is well known from the ICRF coupling theory and experimental studies that the antenna coupling resistance depends on the plasma density [45-47]. The increase of the coupling efficiency with applied RF power during plasma production experiments at fixed gas pressure is in agreement with the theory and indicates a rise of the plasma density with coupled power. The latter is typical for plasmas with non-complete ionization [18, 22, 48].

Another solution for increasing the coupling is based on the effect of FW conversion to SW and IBW in low density/temperature plasmas containing two ion species, e.g. $\text{D}^+ + \text{H}^+$, ${}^4\text{He}^+ + \text{D}^+$ or ${}^4\text{He}^+ + \text{H}^+$. The effect was predicted from modeling with the TOMCAT full wave 1-D RF code [21] accounting for electron (collisional, Landau, TTPM) and ion (collisional, linear cyclotron at $n=1-3$ harmonics) damping mechanisms, tested for the first time in JET [49] and further developed during ASDEX Upgrade ICWC experiments [43]. Generally, the FW may be non-propagating over the plasma cross-section except for the narrow conversion area located close to the fundamental

ion cyclotron resonance (ICR) of the main plasma species, protons ($\omega = \omega_{cH+}$) or deuterons ($\omega = \omega_{cD+}$), depending on the ICWC scenario. In this regime, antenna coupling becomes sensitive to the radial location of the MC layer: the closer this layer is located to the antenna surface the higher the antenna-plasma coupling. This coupling effect is more pronounced for the standard $0\pi0\pi$ -phasing operation ($\eta / \eta_0 > 3$) [43].

Coupling to low density plasmas may also be enhanced by increasing the ion cyclotron harmonic number by ~ 10 times either by decreasing the B_T -value or increasing the generator frequency. In terms of FW excitation, this effect is attributed to a strong shrinking of the SW and FW evanescent layers at the plasma edge [18]. As a result, the FW propagation in low density ICWC plasmas becomes possible even in the high κ_z -spectrum case (Fig.6b), giving rise to the antenna coupling, $\eta / \eta_0 \approx 4$ [44]. One should note, however, that the last solution cannot be realized in ITER at full- or half-field operation with the given frequency band for the ICRF H&CD system (40–55 MHz) and is only useful for very low field operation during commissioning or repair periods.

3.3. ICWC discharge characterization and optimization

Since the gas breakdown phase of the ICRF discharge is considered critical during the fast transition from vacuum to plasma conditions, RF power was applied prior to gas injection during JET-ICWC experiments, in order to avoid gas breakdown inside the antenna box.

It was necessary to pre-match the antenna to a vacuum-near load which is typical to ICRF antenna operation in the low density plasma condition. An example of the transition from the RF breakdown phase (at $t=3.75$ s) to the sustained phase for a typical JET ICWC discharge is shown in Fig.11. The gas breakdown event shows up as an increase in the coupling resistance, a drop in the antenna RF voltage and in a burst in the H_α emission (measured away from the antenna). This correlation, obtained during ICWC discharge initiation, is an indication of successful gas breakdown outside of the antenna box [49].

Further JET-ICWC optimization resulted in a single RF pulse (up to 9s), with a multi-step RF power waveform. Figure 12 shows a typical JET-ICWC pulse with the JET A2 antenna operating in the newly developed plasma production mode as described above. The ICWC discharge formation via robust ionization of the working gas (D_2 , He or their mixtures) and the discharge sustainment with improved homogeneity ($n_e \approx (1-3) \times 10^{11} \text{ cm}^{-3}$) in conditions relevant to the ITER full field (on-axis resonant condition $\omega = \omega_{cD+}$) were achieved in close agreement with the JET safety regulations: multi-step RF pulse was applied first to the magnetized ($B_T=3.3$ T) vacuum torus, followed by a delayed (≈ 0.5 s) pre-programmed injection of the torus gas mixture in order to keep the total pressure down to about 2×10^{-3} Pa during the ICWC sustainment phase.

When the gas reached the antenna-near RF-field, it was successfully ionized resulting in the observed RF power coupling efficiency to the low density plasma (dashed curves) of about 60%. The increase in the loading resistance (detection of the coupled RF power) coincides with the moment of the gas breakdown. Signals from the multi-channel FIR interferometer clearly indicate

the RF plasma presence in the whole cross-section from LFS (antenna side, channels 4-3) towards HFS (channels 2-1). RF plasma ignition was achieved on the first ICWC discharge attempt due to the selected monopole phasing in mode conversion (MC) scenario. Sporadic tripping on antenna power/voltage, as observed during previous ICWC experiments in JET [49], could be avoided by careful antenna pre-matching to vacuum conditions and RF power applying to vacuum torus prior to gas injection.

The RF plasma build-up over the total cross-section of the JET vessel was also confirmed by images from wide-angle (Fig.13) and antenna-viewing (Fig.14) CCD cameras. The visible light image shows the overall improvement of the plasma poloidal homogeneity and its extension towards the divertor by switching on the vertical magnetic field (Fig.13b). The bright vertical zone visible in the plasma images (Fig.14) coincides with the location of the fundamental ICR for deuterons on-axis, $\omega = \omega_{cD+}$. The presence of the fundamental ICR in plasma cross-section plays a crucial role in the ICRF plasma production process based on electron collisional ionization. The resonance triggers a radially extended plasma wave mode conversion (FW \rightarrow SW \rightarrow IBW) in plasmas with several ion species which results in an electron dominant absorption of the RF power. Figure 15 shows an example of modeling with the TOMCAT code [21] of the RF power absorption in a JET multi-ion ICWC plasma, typical for isotope exchange experiments: D₂ gas injection into the vessel with H₂ preloaded walls [14]. Because of the low plasma temperature during the ionization phase ($T_i < T_e \sim 5-10$ eV [5, 41, 49]), the RF power is predicted to be dissipated mostly collisionally. The electrons absorb the largest fraction of the coupled power, $P_{RF-e} \approx (0.75-0.9)P_{tot}$ mainly in the mode conversion zone extending from the on-axis ICR ($\omega = \omega_{cD+}$) towards the HFS due to the presence of the deuterium-hydrogen ion species mixture. The maximum in the plasma density profile of JET D₂-ICWC plasmas correlates with the maximum for the predicted electron power deposition profile, P_{RF-e} , mainly at the HFS in the mode conversion zone thus confirming the basic *electron* collisional ionization mechanism for ICRF plasma production (Fig.16). The higher plasma density typically seen at the LFS, (i.e. where the antenna is located) and also observed in other machines [48, 50] cannot be predicted with the present version of the TOMCAT code and needs further investigation. The ions absorb a minor fraction of the RF power, $P_{RF-i} \approx (0.10-0.25)P_{tot}$, mainly collisionally. In addition, cyclotron absorption by resonant deuterons and hydrogen molecular ions H₂⁺ is predicted at the on-axis fundamental ICR (Fig.15). High energy hydrogen and deuterium CX atom fluxes resulting from the IC absorption were detected in all ICWC experiments that simulated ITER half-field operation scenario, i.e. with on-axis fundamental cyclotron resonance for protons, $\omega = \omega_{cH+} = 2\omega_{cD+}$ undertaken previously on other devices than JET [11, 13, 18, 49]. Interestingly, the high energy D ($\bar{E}_{\perp(D)} \approx 5-20$ keV) and H ($\bar{E}_{\perp(H)} \approx 2-15$ keV) CX atoms were also detected by the NPA diagnostic in the present JET ICWC experiments as well (see Fig.12, also [14]). The possible acceleration mechanisms for the protons in JET ICWC plasmas (fundamental ICR for molecular ions H₂⁺, $\omega = \omega_{cH2+}$, with their further dissociation and/or direct non-linear ICR for the protons at the first sub-harmonic, $\omega = 1/2\omega_{cH+}$, [51]) and role of

the fast particles in the ICWC efficiency will be the subject of further studies.

3.4. Optimization of the wall conditioning efficiency

The conditioning efficiency was studied by measuring the overall outgassing rate of several *marker gases* using mass spectroscopy and/or optical penning gauges. We define the outgassing rate of a given species as the quantity [52]:

$$Q_{RR}(t) \sim V(dp/dt) + p \cdot s + V(\kappa_d + \kappa_i)pn_e \quad (34)$$

Here V is the volume, p and s are the partial pressure of the given mass and its pumping speed, respectively, κ_d and κ_i are the dissociation and ionization rate and n_e is the electron density.

It is known that the ICWC conditioning efficiency increases with increasing gas pressure and coupled RF power [14]. JET safety regulations forced to keep the gas pressure during ICWC experiments at the very low value of 2×10^{-3} Pa, which was never used in the ICWC experiments before. Therefore only the RF power coupled to the plasma was used as a parameter for the optimization of the D₂-ICWC experiments.

Figure 17 gives an example of such an optimization by applying D₂-ICWC in JET with the first wall preloaded with H₂. The increase in the partial pressures for masses 3 (HD) and 2 (H₂) after the RF pulse termination was much higher in the case of antenna monopole phasing (solid lines) compared to super-dipole phasing (dashed lines). The net power coupled to the ICWC plasma was doubled with monopole phasing (for the same generator power) and (possibly partly due to this) a higher and more homogeneous plasma density was obtained. In this way we could maximize the ratio between out-pumping (H) and retained (D) atoms without reducing the H release.

The efficiency for fuel removal by isotopic exchange was assessed using the following procedure: two hours of a H₂ glow discharge to preload the walls with $\approx 4 \times 10^{23}$ H-atoms, after which the JET cryopumps were regenerated. This was followed by 8 nearly identical D₂-ICWC discharges ($p = 2 \times 10^{-3}$ Pa, $B_V = 30$ mT, 9s duration). The cryopumps were then again regenerated and the gas released was analyzed by gas chromatography [14]. The isotopic ratio deduced from midplane spectroscopy, is shown in figure 18 as a function of the cumulated discharge time. The data show a noticeable increase of the isotopic ratio D/(D+H) between 40% and 60% in a cumulated discharge time of 72s. The following averaged isotope exchange efficiency was achieved: H_{outgassed}/D_{implanted} $\approx 1/3$.

The evolution of the antenna coupling and related antenna-near plasma density during the isotope exchange experiments highlighted a dominant role of the mode conversion process in (D+H)-plasmas with variable concentration of the ion species. Both parameters were higher at lower D⁺ concentration (Fig.19), i.e. at the beginning of the D₂-ICWC experiment (Fig.18) and gradually decreased with increasing cumulated conditioning time while the generator power was kept constant. The TOMCAT code predicts a decrease in the fraction of RF power absorbed by the electrons (via a MC process) with increasing D⁺ concentration (Fig.19). To highlight this tendency,

only data of 4 ICWC discharges with the identical RF generator power (380 kW) delivered to the JET A2D antenna from the 8 available conditioning shots (Fig.18) were used in the mentioned analysis (Fig.19). Therefore the lowest values for antenna coupling and plasma edge density coincide implicitly with the lowest H-removal rate and may be used for an alternative monitoring of the surface isotope exchange.

4. ICWC DISCHARGE EXTRAPOLATION TO ITER

As was mentioned in Section 2, electromagnetic waves cannot propagate in the vacuum vessel of present-day tokamaks or stellarators in the typical ICRF band ($\sim 20\text{--}60$ MHz) due to the *small size* of their cross-section relative to the excited wavelength. Therefore the gas breakdown phase of the ICRF discharge, initiated by the antenna-near E_z -field, is considered critical for the operation of ICRF antennas in the plasma production mode because of the fast transition of the antenna loading conditions from vacuum to plasma. However, this cautious condition may be considerably easier and safer in future *large-size* machines keeping in mind the fact that the excited wavelength (for the same ICRF band) will already be comparable with the cross-section size of vacuum vessel and propagation of vacuum electromagnetic waves will be possible. Generally, electromagnetic wave solutions in closed vacuum waveguides may be classified with the *E-waves* (electric type) that contain electric field in the direction of propagation and with the *H-waves* (magnetic type) that contain magnetic field in the direction of propagation [53]. The ICRF plasma production in toroidal fusion machines is based on the acceleration of the electrons in the RF electric field. Therefore, further progress in understanding the neutral gas RF breakdown in large-size fusion machines can be expected from studying the dispersion relation for the *E-waves*. A general solution for Maxwell's equations in a vacuum waveguide in cylindrical coordinates (r, θ, z) results in the following expression for the E_z -field of a positively travelling *E-wave* (in the $+z$ -direction):

$$E_{z(mn)} = E_{z0} J_m(k_r r) \exp(ik_{zn} z + ik_{\theta m} \theta - i\omega t). \quad (35)$$

The required boundary condition is that the tangential electric field should be zero at all conducting surfaces, $E_z(r_0) = 0$. This requires $J_m(k_r r_0) = 0$ and we obtain finally the dispersion relation for the *E-wave*:

$$k_z^2 = \frac{\omega^2}{c^2} - \frac{(m^2 + \alpha_{ml}^2)}{r_0^2}. \quad (36)$$

Here α_{ml} are the roots of the m -th order Bessel function of the first kind, $J_m(\alpha_{ml}) = 0$. The frequency, which determines a threshold for the wave propagation along the waveguide, $\kappa_z^2 = 0$, is called the cut-off frequency, $f_{c-E_{ml}}$:

$$f_{c-E_{ml}} = \frac{c}{2\pi r_0} \sqrt{m^2 + \alpha_{ml}^2}. \quad (37)$$

It is easy to show that the lowest cutoff frequency of all *E-waves* in a given cylindrical waveguide corresponds to the first root of the zero-order Bessel function, $\alpha_{01} = 2.405$: $f_{c-E_{01}} = 1.147 \times 10^8 r_0^{-1}$ (Hz). A further increase in the generator frequency ($f > f_{c-E_{ml}}$) results in the *E-wave* propagation along the waveguide with parallel wave-vector $\kappa_z^2 > 0$, satisfying to vacuum dispersion relation (Eq. (36)). The present analysis clearly shows that the boundary condition for guided electromagnetic waves results in a quantization of the radial and poloidal wavenumbers: an infinite set of discrete values for κ_r and κ_θ is allowed [24, 53]. Considering the vacuum torus as a straight cylinder of the length $L = 2\pi R_0$ with identical ends, we obtain also a discretization of the toroidal mode numbers needed to achieve a standing wave pattern formed by the superposition of incident and reflected waves. Therefore the *resonant excitation* of the high-Q cavity modes (eigenmodes) in the vacuum torus (E_{mln} -modes) may be achieved at frequencies $f_{E_{mln}}$ determined by discrete values of the poloidal, radial and toroidal wave vectors [53]:

$$f_{E_{mln}} = \frac{c}{2\pi} \sqrt{\frac{m^2}{r_0^2} + \frac{\alpha_{ml}^2}{r_0^2} + \frac{n^2}{R_0^2}} . \quad (38)$$

Here n and m are the integer toroidal and poloidal mode numbers (number of wavelength variations in toroidal/poloidal directions), l is the integer ($\neq 0$) number of half-wavelength variations from wall to wall in radial direction, R_0 and r_0 are the major and minor radii of the torus, respectively.

Modeling of the electromagnetic wave propagation for the ITER-like D-shaped *vacuum* torus was undertaken with the 3-D MWS code [20]. The eigenmode solver predicts a frequency threshold for the *E-wave* excitation and vacuum eigenmode formation in the frequency range $\approx 43\text{-}44$ MHz (Figs.20,21), which is fortunately in the frequency band for the ITER ICRF H&CD system.

Further analysis shows that the numerically found frequency for the homogeneous distribution of the E_z -field along the ITER-like torus ($f_{E_{010}} = 42.9807$ MHz) corresponds to the cut-off frequency of the E_{010} -mode excitation in cylindrical waveguide ($n_{\text{tor}}=0$) with effective radius $r_{0-\text{eff}} \approx 0.91\sqrt{r_v r_h}$, where $r_v \approx 394$ cm and $r_h \approx 220$ cm are the ITER vessel vertical and horizontal radii, respectively. The first global (E_{011} cavity mode, $n_{\text{tor}}=1$) resonance is predicted to be excited at frequency $f_{E_{011}} = 43.8469$ MHz slightly shifted from the threshold frequency $f_{E_{010}}$. Therefore careful fine-tuning of the RF generator to resonant excitation of the cavity modes is necessary. The result of ITER gas breakdown analysis is shown for the standard case of non-propagating (evanescent) electromagnetic waves in a vacuum torus ($f=40$ MHz) in Fig.22 and for the regime with torus cavity mode formation ($f_{E_{010}} = 42.9807$ MHz) in Fig.23. The new regime demonstrates several principal advantages for safe and reliable performance of the gas breakdown in ITER compared to the “standard evanescent” regime:

- Ability to start ionization in the vessel core at ultra-low RF voltage at the antenna strap ($V_{\text{RF-strap}} \approx 2.5$ kV);
- Potential to achieve ionization over the total cross-section at moderate RF voltage ($V_{\text{RF-strap}} \approx 15$ kV);

- Performance of gas breakdown entirely outside the antenna box due to boundary condition $E_z = 0$ at all conducting surfaces;
- Simultaneous breakdown in the full torus due to vacuum eigenmode formation.

This newly discovered effect gives evidence that the gas breakdown and initial ionization may occur in ITER simultaneously over the whole torus. It should note that the promising regime with the cavity modes excited in vacuum torus will exist during a short moment of the neutral gas breakdown. We may expect that the *globally generated* RF plasma will play a double role: destroy the vacuum cavity modes and set up the condition of plasma wave excitation in the toroidal plasma ($\omega_{pe} \geq \omega$) within a short time scale. However the latter is very important for ICRF antenna safe operation during vacuum-plasma transition phase and can considerably facilitate the ICWC operation even at high frequencies. Extrapolation of the vacuum eigenmode solutions from the present-size fusion machines to ITER indicates that the discovered effect can be tested only in a vessel with the size of ITER: the small size of the cross-section in present-day toroidal fusion machines requires operation at much higher frequencies that are not available at their ICRF systems (Fig.24).

An upgraded 0-D plasma code [22] was used to estimate the RF power necessary to produce and sustain ICWC hydrogen/deuterium plasmas in ITER ($\alpha_{pl} \approx 240$ cm, $R_0 = 620$ cm) at $B_T = 5.3$ T in the pressure range $p \approx (2-8) \times 10^{-2}$ Pa. The code predicts that RF plasmas with a density $n_e \approx (1-5) \times 10^{11}$ cm⁻³, electron temperature $T_e \approx 1-2$ eV and ionization degree $\gamma_i \approx 0.05-0.10$ can be produced with a power $P_{pl-ITER} \approx 0.3-1.5$ MW coupled to the electrons depending on the gas pressure. Assuming an "optimistic" antenna coupling efficiency $\eta \geq 0.5$ at monopole-phasing, this corresponds to a generator power $P_{G-ITER} \approx 0.6-3.0$ MW. A direct extrapolation from the TEXTOR and JET ICWC data (coupled power $P_{pl-TEXTOR} \approx 12-30$ kW, $P_{pl-JET} \approx 230$ kW, assuming a *similar power density* scaling and antenna coupling) gives a power of $P_{pl-ITER} \approx 1-2$ MW and $P_{G-ITER} \approx 2-4$ MW, respectively. Interestingly, the amount of RF power needed to sustain the ICWC discharge in ITER as predicted by the 0-D plasma code and obtained from the direct extrapolation to ITER as outlined above was found in a reasonable agreement with another extrapolation of the ICWC power needed for ITER, based on the ratio of the PFC surfaces (~ 3.5 MW) [3].

The TOMCAT 1-D RF code [21] predicts that a more homogeneous power absorption by the electrons over the ITER vessel may be achieved in the MC scenario at intermediate $B_T = 3.6$ T with two different frequencies ($f_1 = 40$ MHz and $f_2 = 48$ MHz) and low κ_z -spectrum ($\pi/3$ -, $\pi/6$ - or *monopole*-phasing between the RF currents in the toroidally adjacent antenna modules). Performance of the MC scenario at half-field ($B_T = 2.65$ T) or at full field ($B_T = 5.3$ T) may result in a less homogeneous ICWC discharge. However, plasma production with an antenna phased to low κ_z -spectrum of the radiated RF power is beneficial: (i) the FW is already propagating in low density plasmas; (ii) better antenna coupling is foreseen; (iii) larger fraction of the coupled RF power may be transported to a distant (>2 m) mode conversion layer.

CONCLUSION

Recent progress is presented in the understanding of the basic processes responsible for gas

breakdown and ICRF plasma production, and in the modeling, characterization of antenna coupling and establishing of the parameters for ICWC plasmas targeted on the increase of the wall conditioning efficiency.

These studies resulted in:

1. Further development of a consistent model for RF plasma production in a magnetized torus comprising pre-wave and wave phases of gas ionization, plasma build-up and sustain using standard ICRF antenna.
2. Working out a general approach for ICRF antenna operation in the plasma production mode and establishing reliable working parameters (antenna RF voltage and power, frequency, phasing and gas pressure) needed for efficient wall conditioning.
3. First successful simulation of the ITER full field ICWC scenario in the largest present-day tokamak JET.
4. Demonstration of the principle possibility to make use of the currently planned ITER ICRF HCD system for ICWC applications based on simulations with 3-D electromagnetic, 1-D RF and 0-D plasma codes and complimented by direct extrapolation of the experimental data obtained on the present-day tokamaks.

ACKNOWLEDGMENTS

One of the authors (F.C.S.) wants to acknowledge the support of his work for this publication by ITER-IO through Contract No IO/2009/ADM-014. This work was supported by EURATOM and carried out within the framework of the European Fusion Development Agreement. The views and opinions expressed herein do not necessarily reflect those of the European Commission.

REFERENCES

- [1]. Winter J. 1996 *Plasma Physics and Controlled Fusion* **38** 1503
- [2]. Philipps V. *et al* 2008 22th IAEA Fusion Energy Conf. (Geneva 2008) Paper FT/4-2Ra
- [3]. Shimada M, Pitts R.A. 2011 *Journal of Nuclear Materials* **415** S1013-S1016
- [4]. Esser H.G. *et al* 1997 *Journal of Nuclear Materials* **241–243** 861
- [5]. Gauthier E. *et al* 1997 *Journal of Nuclear Materials* **241–243** 553-558
- [6]. Zhao Y.P. *et al* 1997 *Chinese Physics Letters* **14** 916
- [7]. Hu J S *et al* 2008 *Journal of Nuclear Materials* **376** 207-210
- [8]. Hong S.H. *et al* 2010 23rd IAEA Fusion Energy Conf. (Daejeon 2010) Paper EXD/P3-17
- [9]. Nazarov N.I. *et al* 1987 *Soviet Journal of Plasma Physics* **13** 871-873
- [10]. Brakel R. *et al* 2001 *Journal of Nuclear Materials* **290–293** 1160-1164
- [11]. Ashikawa N. *et al* 2006 *Fusion Engineering and Design* **81** 2831-2836
- [12]. Moiseenko V.E. *et al* 2011 *Nuclear Fusion* **51**, doi:10.1088/0029-5515/51/8/083036
- [13]. de la Cal E, Gauthier E. 2005 *Plasma Physics and Controlled Fusion* **47** 197-218
- [14]. Douai D. *et al* 2011 *Journal of Nuclear Materials* **415** S1021-S1028
- [15]. Beaumont B. *et al* 2009 23rd IEEE/NPSS Symposium on Fusion Engineering (San Diego 2009)
- [16]. Carter M.D. *et al* 1990 *Nuclear Fusion* **30** 723-730
- [17]. Lyssoivan A. *et al* 1992 *Nuclear Fusion* **32** 1361-1372

- [18]. Lyssoivan A. *et al* 1998 *Final Report on ITER Design Task D350.2 LPP-ERM/KMS Laboratory Report No 114*
- [19]. Lyssoivan A. *et al* 2010 *Problems of Atomic Science and Technology* **6** Series: Plasma Physics **16** 46-50
- [20]. Weiland T, Timm M. and Munteanu I. 2008 *IEEE Microwave Magazine* **9** 62-75
- [21]. Van Eester D. and Koch R 1998 *Plasma Physics and Controlled Fusion* **40** 1949-1975
- [22]. Wauters T. *et al* 2011 *Plasma Physics and Controlled Fusion* **53** 1-20
- [23]. Shvets O.M. *et al* 1984 *4th Int. Con. On Heating in Toroidal Plasmas* Vol.**1** 513-528
- [24]. Stix T. 1992 *Waves in Plasmas*. N.Y. „Springer-Verlag“
- [25]. Koch R. 2006 *Transactions of Fusion Science and Technology* **49** 177-194
- [26]. Kaye A. *et al* 1994 *Fusion Engineering and Design* **24** 1
- [27]. Gould L. and Roberts L.W. 1956 *Journal of Applied Physics* **27** 1162-1170
- [28]. Golant V.E. 1958 *Uspekhi Fizicheskikh Nauk* **65** 39-89
- [29]. Piel A 2010 *Plasma Physics: An Introduction to Laboratory, Space and Fusion Plasmas*. „Springer-Verlag Berlin Heidelberg“
- [30]. Swanson D.G. 1989 *Plasma Waves*. “Academic Press, Inc. London”
- [31]. Bender C.M. and Orszag S.A. 1978 *Advanced Mathematical Methods for Scientists and Engineers*. McGraw-Hill, N.Y. 560.
- [32]. Schüller F.C. *et al* 2010 *Report on Applications of ICWC on ITER*, Private Communication
- [33]. Shvets O.M, Lyssoivan A I 1977 *Gas RF breakdown in the U-1M stellarator*, Private Communication
- [34]. Longinov A.V, Stepanov K.N. 1992 in *High-Frequency Plasma Heating* N.Y. 93-238
- [35]. Ono M, Wong K.L. and Wurden G.A. 1983 *Physics of Fluids* **26** 298-309
- [36]. Van Eester D, Louis Y and Koch R. 1993 *Plasma Physics and Controlled Fusion* **35** 1189
- [37]. Lyssoivan A. *et al* 2007 *Journal of Nuclear Materials* **363-365** 1358-1363
- [38]. Korzh A.F, Stepanov K.N. 1987 *Soviet Journal of Plasma Physics* **13** 164
- [39]. Wauters T. 2011 *PhD Thesis* Gent University Belgium, ISBN 978-90-8578-458-6
- [40]. Wauters T. *et al* 2009 *18th Topical Conf. on RF Power in Plasmas (Gent 2009)* AIP/CP-1187 N.Y. 173-176.
- [41]. Vicente C. *et al* 2005 *IEEE* 1055-1058
- [42]. Anza S. *et al* 2010 *Physics of Plasmas* **17** 062110(1-11)
- [43]. Lyssoivan A. *et al* 2009 *Journal of Nuclear Materials* **390-391** 907-910
- [44]. Lyssoivan A. *et al* 2011 *Journal of Nuclear Materials* **415** S1029-S1032
- [45]. Koch R. *et al* 1986 *Computer Physics Communications* **40** 1-22
- [46]. Koch R. *et al* 1988 *Plasma Physics and Controlled Fusion* **30** 1559-1570
- [47]. Messiaen A. *et al* 1989 *Plasma Physics and Controlled Fusion* **31** 921-939
- [48]. Paul M.K. *et al* 2012 *Fusion Engineering and. Design*, **87** 98-103
- [49]. Lyssoivan A. *et al* 2005 *Journal of Nuclear Materials* **337-339** 456-460
- [50]. Douai D. *et al* 2010 *23rd IAEA Fusion Energy Conference (Daejeon 2010)* Paper FTP/P1-26
- [51]. Kitsenko A.B, Pankratov I.M. and Stepanov K.N. 1975 *Sov. Phys.-JETP* **40** 860-864
- [52]. Wauters T. *et al* 2011 *Journal of Nuclear Materials* **415** S1033-S1036
- [53]. Ramo S, Whinnery J.R. and Van Duzer T 1965 *Fields and Waves in Communication Electronics* John Wiley & Sons, Inc., New York–London–Sydney

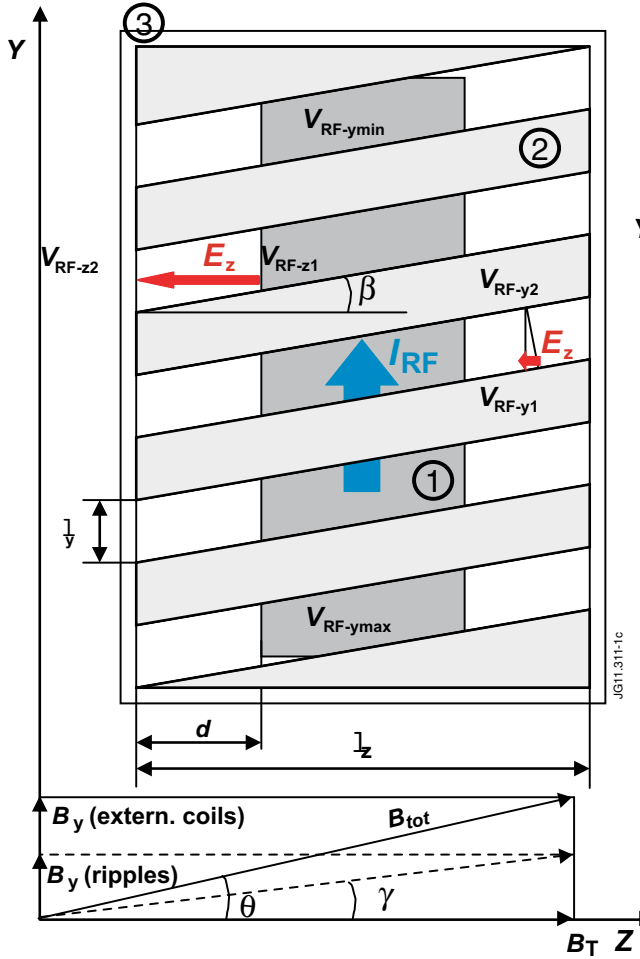


Figure 1. Scheme for E_z -field generation by standard ICRF antenna in vacuum: (1) antenna strap with RF current; (2) Faraday screen rods; (3) antenna box.

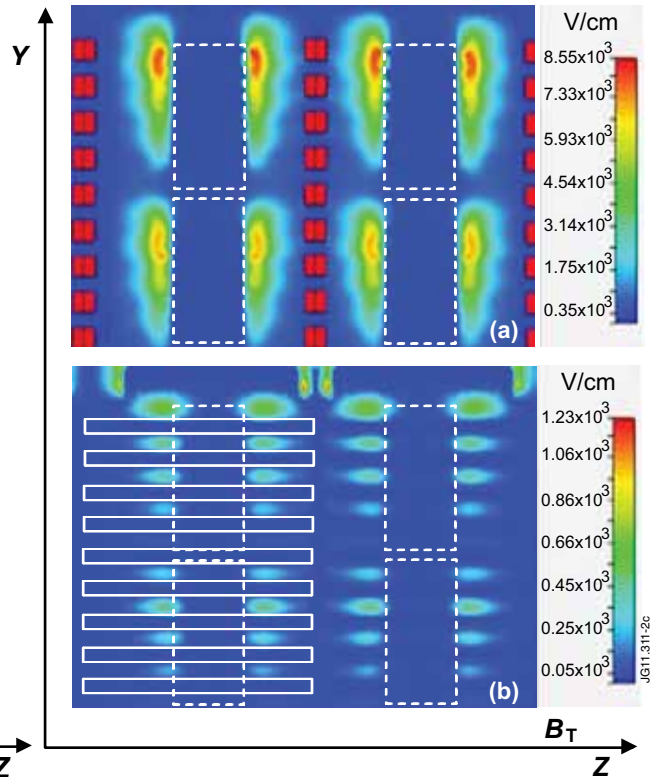


Figure 2. E_z -field simulation for the four straps of ITER multi-strap (24 array) ICRF antenna with 3-D MWS code: (a) inside antenna box at $r=1$ cm from strap (the fat vertical dashed red lines represent the antenna private limiters), (b) outside at $r=1$ cm from FS. Antenna strap locations are shown schematically with vertical (dashed) white contours and FS - with horizontal (solid) white contours ($V_{RF\text{-strap}}=15$ kV, $f=48$ MHz, $\pi/6$ -phasing).

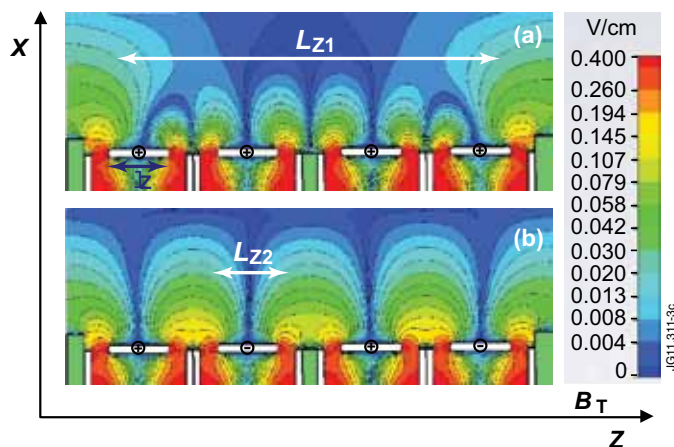


Figure 3. Contour plot for E_z -field pattern in $(x-z)$ -coordinates simulated with the MWS code for ITER antenna ($f=40$ MHz, $P_{RF\text{/strap}}=0.33$ W): (a) - monopole (0000)-phasing, (b) - dipole ($0\pi0\pi$)-phasing.

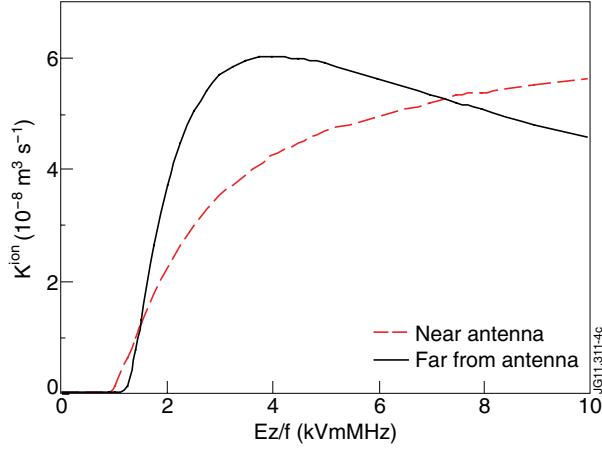


Figure 4. The ionization rate per molecule H_2 near the antenna within the area L_z (red) due to oscillatory movement of the electrons and the same outside L_z (blue) due to the ponderomotive drift as function of the E_z/f -ratio [32].

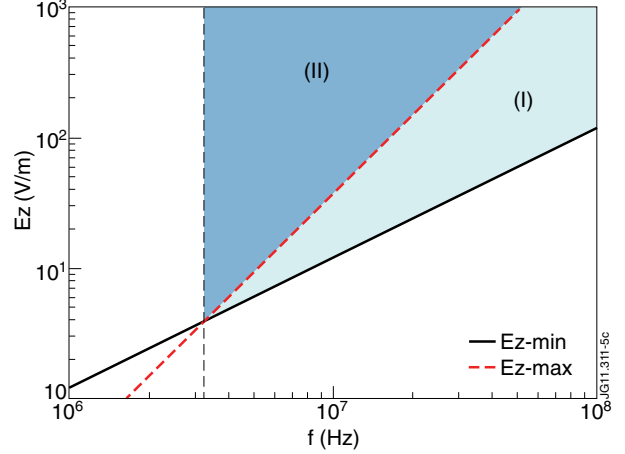


Figure 5. Hydrogen RF breakdown diagram in (E_z, f) -parameter space with two ionization zones: (I) – gas breakdown with trapped and non-trapped (repelled-out) electrons, (II) – gas breakdown with non-trapped (escaped and repelled-out) electrons. The upper threshold for trapped electrons ($E_{z\text{-max}}$ -line) is plotted for the JET A2 antenna powered in monopole phasing, $p_{H_2}=2\times 10^{-3}$ Pa.

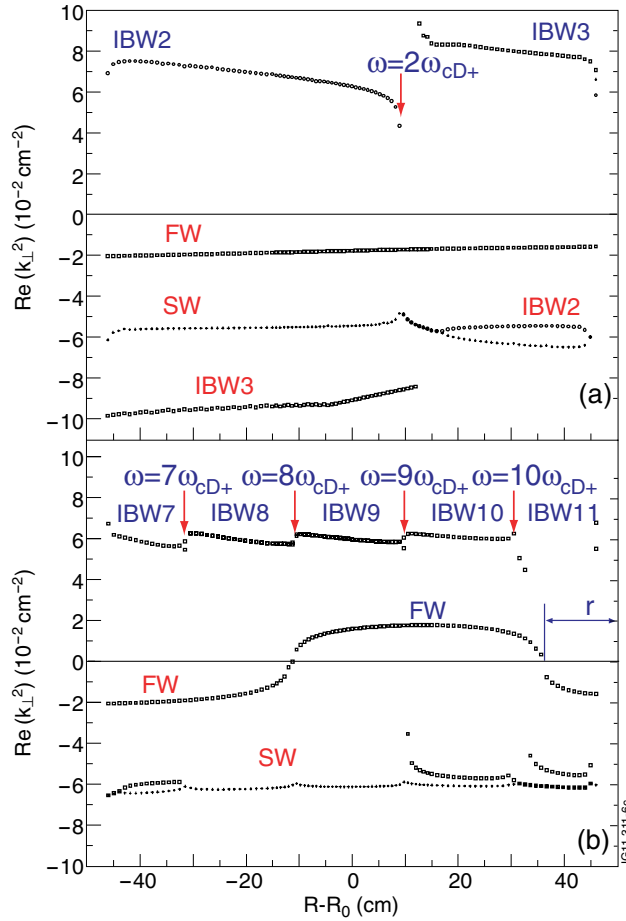


Figure 6. Plasma waves dispersion diagram, $\text{Re}(k_\perp^2)$, in logarithmic scale for the case of TEXTOR D_2 plasma ($n_{e0}=1\times 10^{12} \text{ cm}^{-3}$) in high $B_T=2.24 \text{ T}$ (a) and low $B_T=0.5 \text{ T}$ (b) ($f=32.5 \text{ MHz}$, dipole phasing $\rightarrow k_\parallel(R_0+a)=0.06 \text{ cm}^{-1}$).

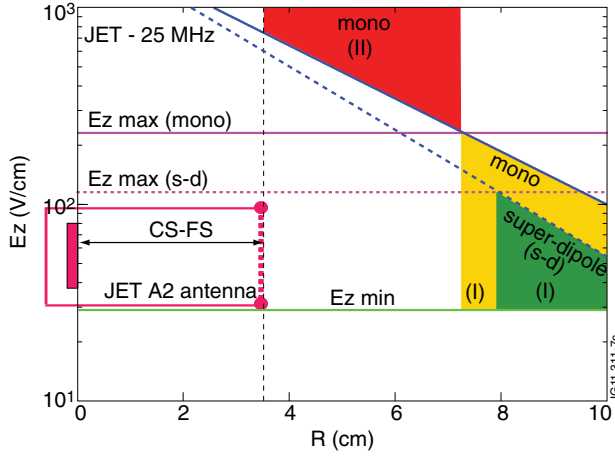


Figure 7. Radial location of RF breakdown zones in H_2 (D_2) gas calculated for JET A2 antenna geometry: (I) – ionization with trapped and non-trapped (repelled-out) electrons (Eq.(19)), (II) – ionization with non-trapped (escaped and repelled-out) electrons (Eq.(20)) at $f=25\text{ MHz}$, $V_{RF\text{-strap}}=15\text{ kV}$, $p_{H_2}=2\times 10^{-3}\text{ Pa}$ and different phasing: monopole (0000) or super-dipole, s-d, (00 $\pi\pi$).

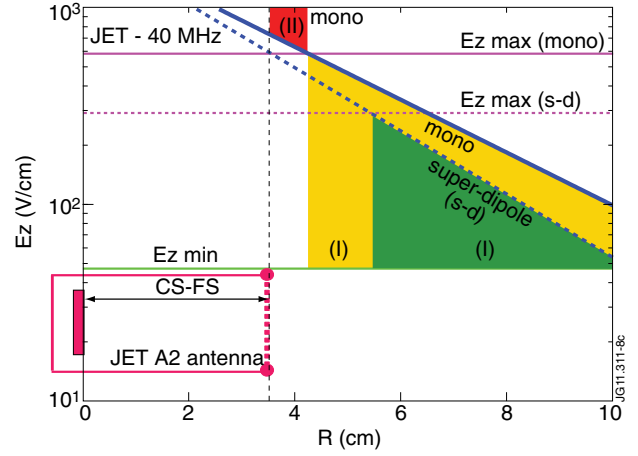


Figure 8. H_2 (D_2) RF breakdown diagram with the same RF voltage, phasing and gas pressure $p_{H_2}=2\times 10^{-3}\text{ Pa}$ as shown in Fig. 7 but at higher frequency $f=40\text{ MHz}$

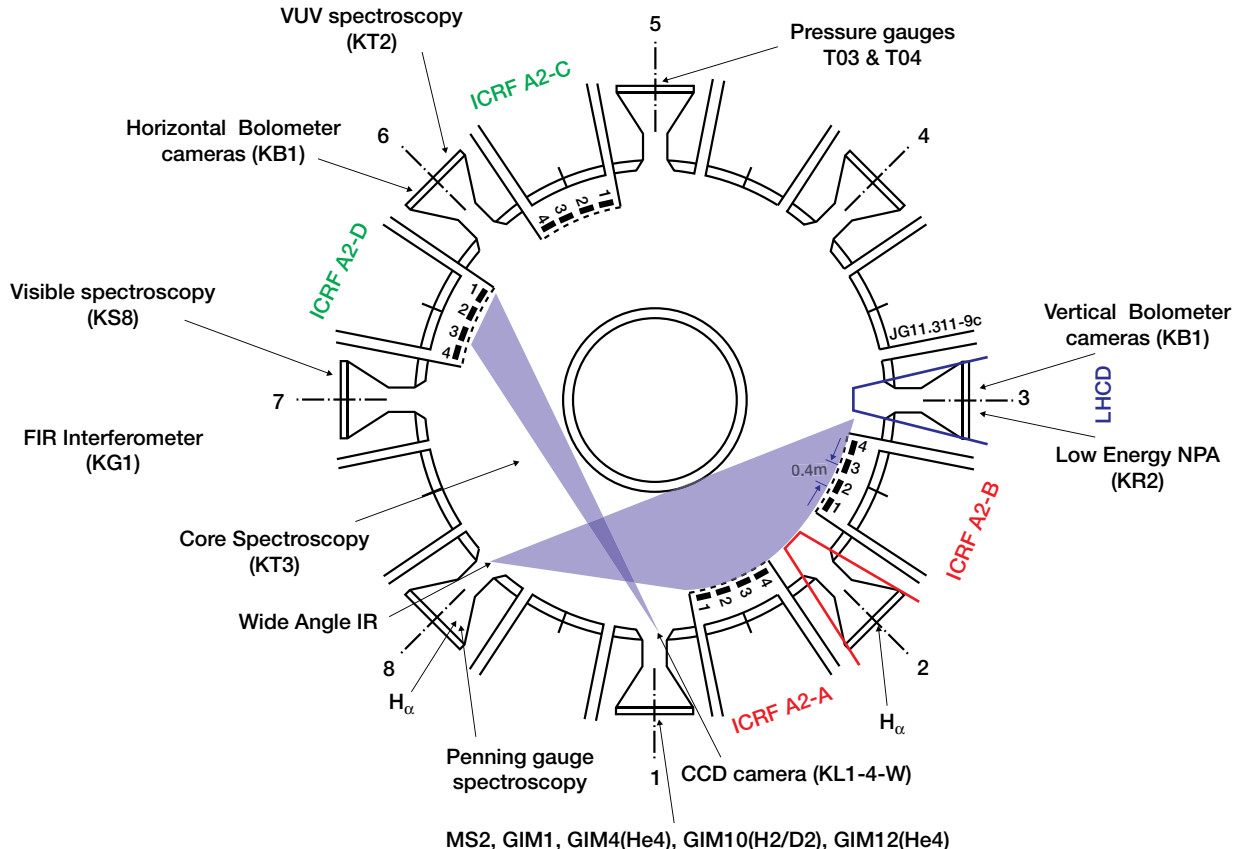


Figure 9. Layout of JET ICRF antennas (highlighted in green) and diagnostics involved into ICWC experiment.

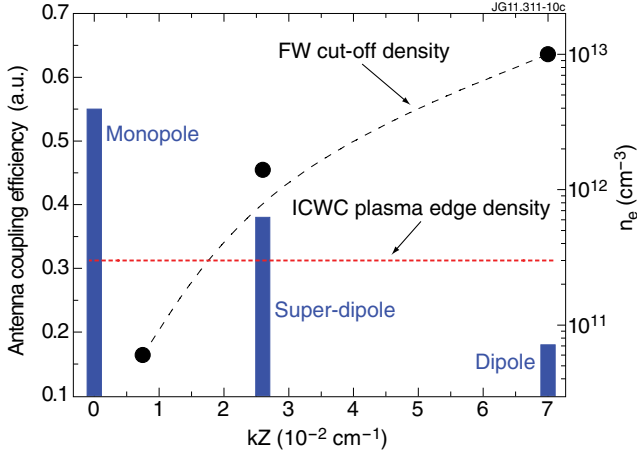


Figure 10. JET A2 antenna coupling to low density ($n_e(a) \approx 3 \times 10^{11} \text{ cm}^{-3}$) ICWC plasmas as a function of the antenna phasing and FW cut-off density ($f=25 \text{ MHz}$, deuterium, $B_T=3.3 \text{ T}$). The blue bars indicate the coupling efficiency for different phasing of the 4 strap antenna.

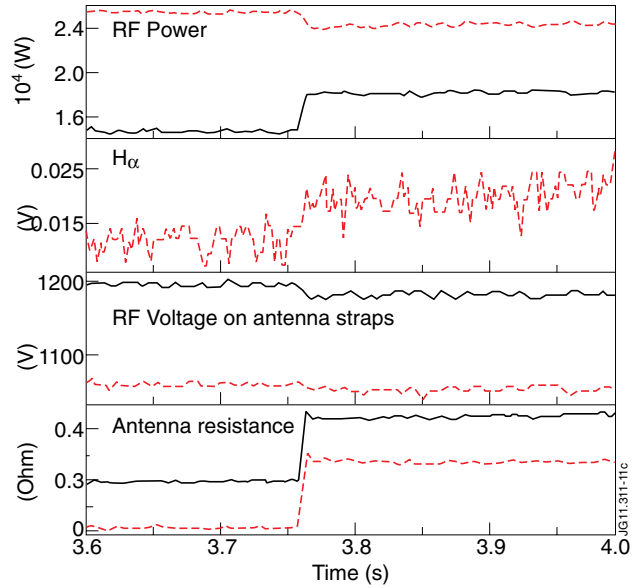


Figure 11. Experimentally observed indications of gas breakdown with JET A2 antennas in a safe manner: drop in antenna RF voltage, rise in antenna resistance and concomitant rise in H_α signal (Pulse No. 79322, A2C (black) and A2D (red) antennas).

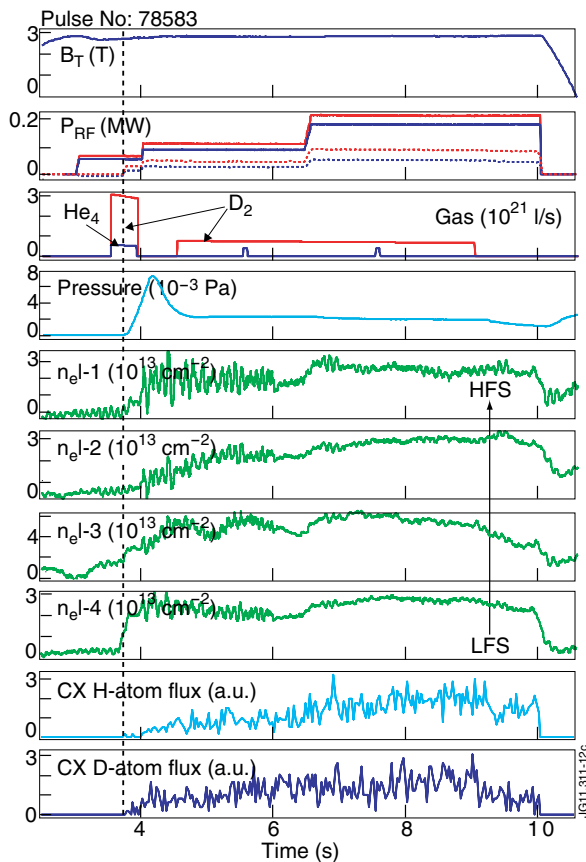


Figure 12. Typical performance of ICWC discharge in JET using ICRF A2 antennas C and D operated in monopole phasing in conditions similar to ITER full field: $f=25 \text{ MHz}$, $P_{RF-G\text{-max}} \approx 400 \text{ kW}$, $h \approx 0.6$, $B_T=3.3 \text{ T}$, $p_{tot}=2 \times 10^{-3} \text{ Pa}$, gas composition – $D_2:He \approx 0.85:0.15$. From top to bottom: Toroidal magnetic field, ICRF power (solid lines correspond to generator power (A2-C – bleed, A2-D – red), dashed lines – to RF power coupled to plasma, respectively), Gas injection from modules GIM-1 (D_2) and GIM-4 (He), Pressure from gauge TO4, Line integrated density from FIR interferometer at 189 cm (n_{el1}), 270 cm (n_{el2}), 304 cm (n_{el3}), 374 cm (n_{el4}), Charge exchange H and D atom fluxes from neutral particle analyzer.

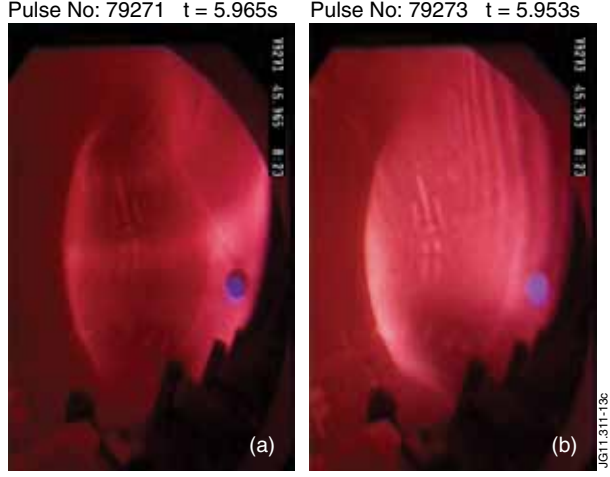


Figure 13. JET D_2 -ICWC plasma images from wide-angle CCD camera looking towards antennas A and B: (a) $B_V=0$ mT (Pulse No: 79271), (b) $B_V=30$ mT (Pulse No: 79273). ICWC regime: $A2C+A2D$ at $f=25$ MHz, monopole phasing, $P_{RF-c} \approx 250$ kW, $B_T=3.3$ T and $p_{tot} \approx 2.0 \times 10^{-3}$ Pa.

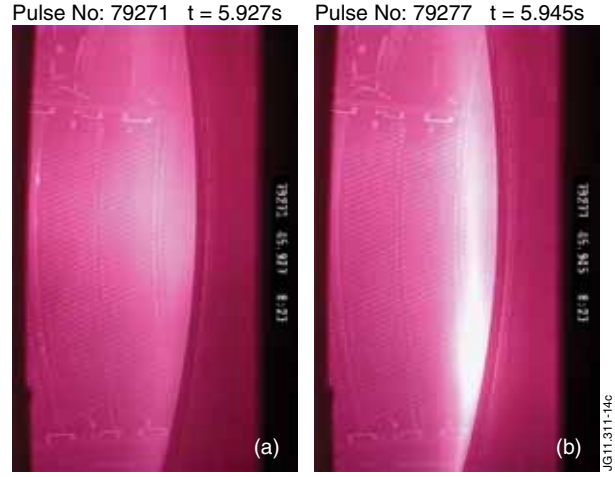


Figure 14. JET D_2 -ICWC plasma images from CCD camera looking at antenna D, straps 1 and 2: (a) $B_V=0$ mT (Pulse No: 79271), (b) $B_V=15$ mT (Pulse No: 79277). Operation regime: $f=25$ MHz, monopole phasing, $P_{RF-G}=2 \times 400$ kW, $B_T=3.3$ T.

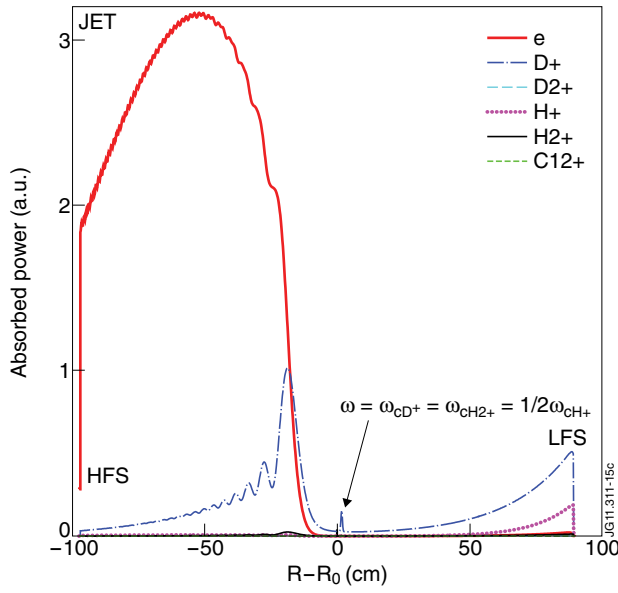


Figure 15. Absorbed power $P_{RF-e}(r)$ and $P_{RF-i}(r)$ simulated for JET-like ICWC plasmas: 56% D^+ :40% H^+ :2.0% D_2^+ :1.5% H_2^+ :0.5% C_{12}^+ ; $n_e \approx 2.5 \times 10^{11}$ cm $^{-3}$, $k_z(0) \approx 0.03$ cm $^{-1}$.

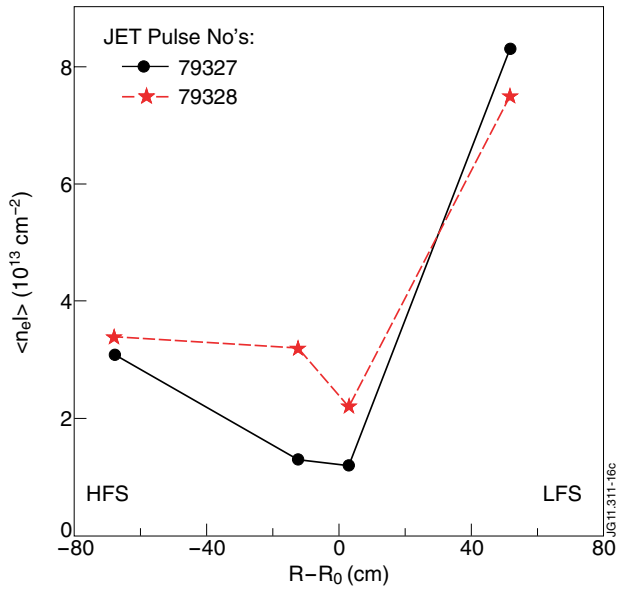


Figure 16. Line-integrated RF plasma density profile measured in JET ICWC conditions: $B_T=3.3$ T, $p_{D2}=2 \times 10^{-3}$ Pa, $A2D$ and $A2C$ antennas at $f=25$ MHz, monopole phasing, $P_{pl-tot} \approx 250$ kW, $n_D/(n_D+n_H) \approx 0.58-0.60$.

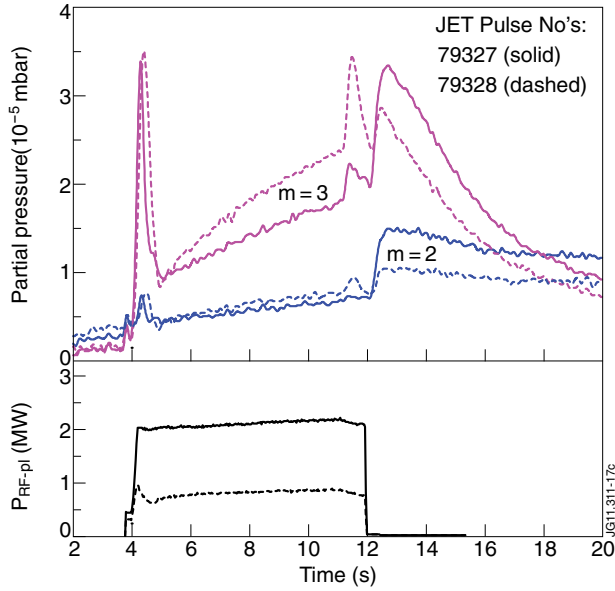


Figure 17. Effect of the antenna k_z -spectrum on JET D_2 -ICWC output (H_2 preloaded): 0000-phasing (shot #79274, solid curve) vs. $00\pi\pi$ -phasing (shot #79276, dashed curve), $f=25$ MHz, $B_T=3.3$ T, $p \approx 2 \times 10^{-3}$ Pa, partial pressure for masses $m=2$ and $m=3$ from penning gauge spectroscopy).

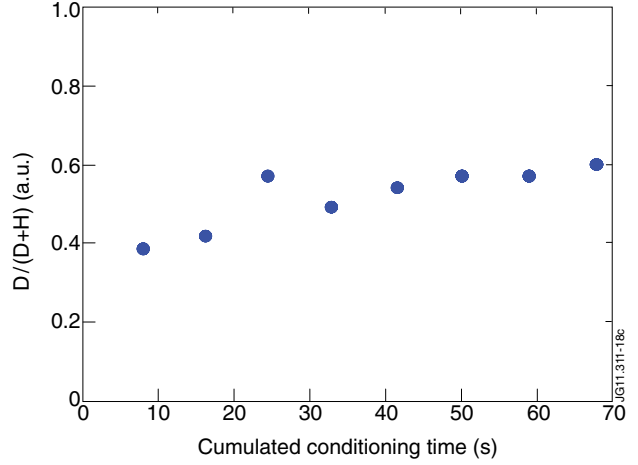


Figure 18. Evolution of the isotopic ratio as a function of the cumulated JET D_2 -ICWC discharge time measured via visible midplane spectroscopy.

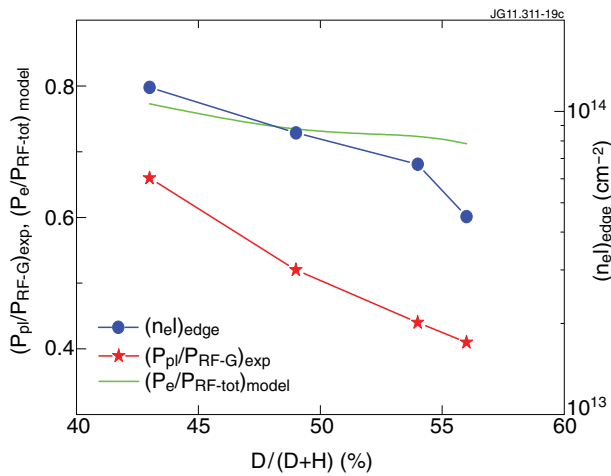


Figure 19. Correlation between A2D antenna coupling, plasma edge density at LFS (antenna side) measured during JET ICWC isotope exchange experiment ($P_{RF-G} \approx 380$ kW, $f_{A2D}=25.21$ MHz, monopole phasing, $B_T=3.3$ T) and fraction of the electron absorbed power predicted by TOMCAT code.

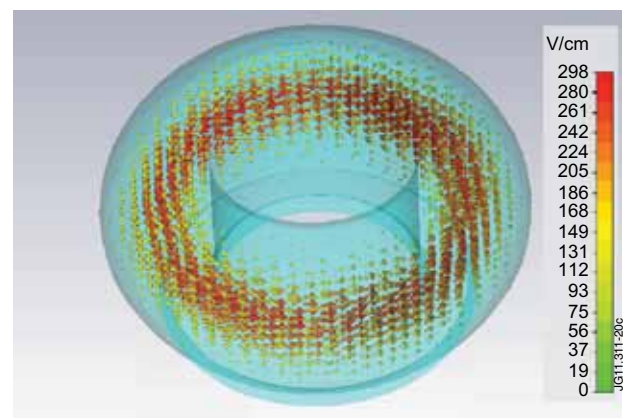


Figure 20. 3-D MWS eigenmode solver: E_z -field distribution along the torus in ITER-like vacuum vessel at a cut-off frequency ($n_{tor}=0$) for the E_{010} -mode propagation ($f_{E010}=42.98$ MHz, all eigenmode solutions are normalized to 1 Joule total stored energy).

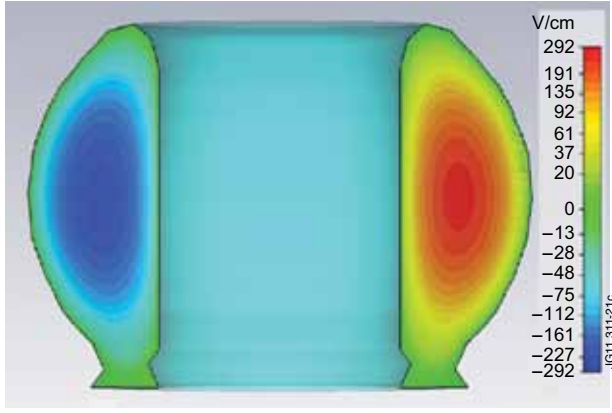


Figure 21. 3-D MWS eigenmode solver: radial distribution of E_z -field for vacuum cavity mode E_{010} excitation in ITER-like vessel at cut-off frequency ($f_{E010}=42.98\text{MHz}$, normalization to 1 Joule total stored energy).

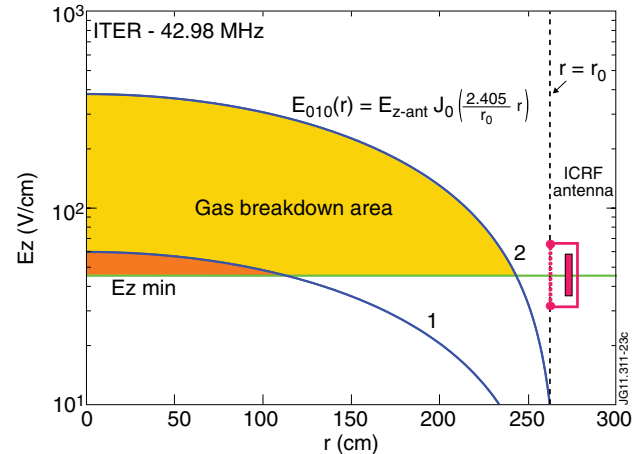


Figure 22. Modeling of radial location of H_2 (D_2) breakdown zone with ITER ICRF antenna operated in “vacuum evanescent wave” regime: (I) – ionization zone with trapped and non-trapped (repelled-out) electrons, (II) – ionization zone with non-trapped (escaped and repelled-out) electrons at $f=40\text{ MHz}$, $V_{RF\text{-strap}}=20\text{ kV}$, $p_{H_2}=2\times 10^{-3}\text{ Pa}$ and different phasing: monopole (0000) or super-dipole ,s-d, (00 $\pi\pi$).

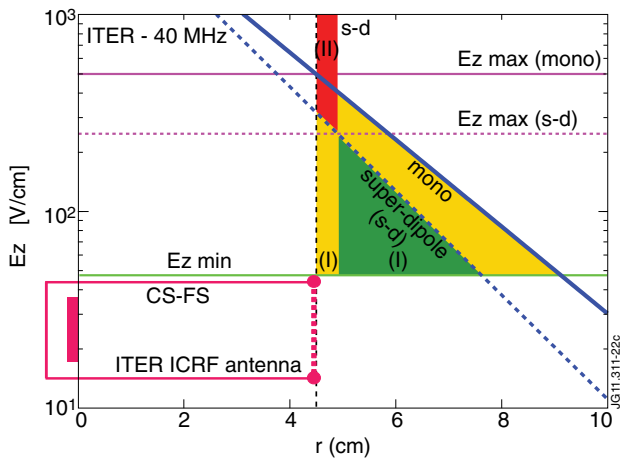


Figure 23. Hydrogen RF breakdown condition in ITER-size vessel with ICRF antenna tuned to excitation of vacuum cavity mode E_{010} (cylindrical approximation: $r_{ant}=r_0\approx 268\text{cm}$, $f_{E010}=42.98\text{MHz}$, $V_{RF\text{-strap}}=2.5\text{kV}$ (curve 1), $V_{RF\text{-strap}}=15\text{kV}$ (curve 2), $p_{H_2}=2\times 10^{-3}\text{ Pa}$. Here r -coordinate starts from the center of torus vessel but not from the antenna strap surface as was used in the “vacuum evanescent wave” regime shown in Fig.22 (also in Figs.7-8).

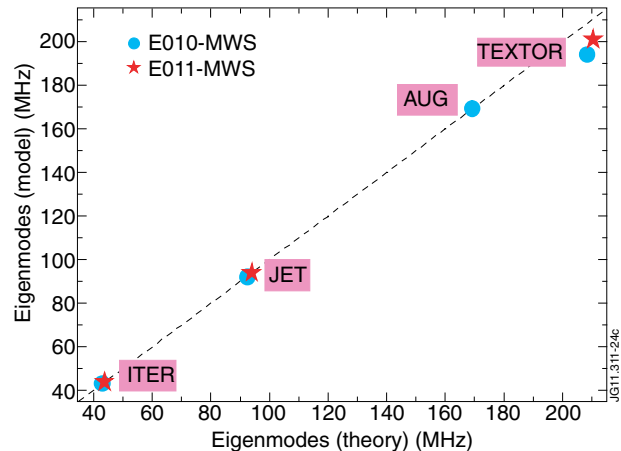


Figure 24. Extrapolation of vacuum eigenmode solutions from the present-size fusion machines to ITER vessel as predicted by MWS modeling for torus with non-circular (D-shaped) cross-section (symbols) and theory of cavity mode excitation in torus with equivalent circular cross-section (dashed line).